Sampling Earth's mantle at intra-transform spreading ridges

Camilla Sani [a,b,*], Alessio Sanfilippo [b], Sergey Skolotnev [c], Marco Ligi [d], Felix Genske [a], Andreas Stracke [a]

[a] Institut für Mineralogie, Universität Münster, Corrensstraße 24, D-48149 Münster, Germany
[b] Dipartimento di Scienze della Terra e dell'Ambiente, Università di Pavia, via Ferrata 1a, 27100 Pavia Italy
[c] Geological Institute, Russian Academy of Science, Pyzhevsky Iane 7, 119017 Moscow, Russia
[d] Istituto di Scienze Marine, Consiglio Nazionale delle Ricerche, via Gobetti 101, 40129 Bologna, Italy

ABSTRACT

The Doldrums transform system, located in the Equatorial Atlantic at 7–8°N, is a 110 km-wide multi-fault shear zone, with five active transform faults separated by four short intra-transform ridge segments (ITRs). The two central ITRs, ITR-2 and ITR-3, are significantly deeper than the peripheral ridge segments, suggesting differences in the thermal conditions of the sub-ridge mantle. New chemical and radiogenic isotope data from on-axis lavas erupted across the transform domain reveal that the basalts from ITR-3 are enriched in alkalis ($Na_2O + K_2O$ = 4.3 wt%; Na_8 up to 3.7) and light rare earth elements $(La/Sm)_N$ = 0.86–0.97). However, these basalts have lower Sr and Pb isotope ratios than MORB from the Equatorial Atlantic (i.e., $^{87}Sr/^{86}Sr \sim$ 0.70237 and $^{206}Pb/^{204}Pb \sim$ 18), and relatively high Nd and Hf isotope ratios ($^{143}Nd/^{144}Nd$ = 0.51315–0.51325; $^{176}Hf/^{177}Hf$ = 0.2832–0.28325). Hence, the mantle underlying ITR-3 is, on average, depleted in highly incompatible elements. Thermal models of the sub-ridge mantle show that it is also the coldest mantle region under the Doldrums system with the lowest crust production. Considering its location in the central transform domain, it is likely that the local mantle underwent melting beneath adjacent segments of the Mid-Atlantic Ridge (MAR) before remelting below ITR-3. We propose that the initial melting event beneath the MAR selectively removed the most fusible, geochemically enriched mantle components, leaving behind a predominantly peridotitic source, characterized by comparatively low Sr and Pb isotope ratios. Therefore, MORB from intra-transform ridge segments, such as those within the Doldrums transform system, provide a rare opportunity to constrain the isotopic composition of highly incompatible element depleted peridotitic mantle, which is a ubiquitous, but otherwise often camouflaged component of Earth's mantle.

1. Introduction

Mid Ocean Ridge Basalts (MORB) are partial melts of Earth's upper mantle. The upper mantle is a mixture of heterogeneous peridotites that have experienced variable degrees of incompatible element depletion during previous melting events and incompatible element-enriched materials, primarily recycled oceanic and continental crust (e.g., Stracke, 2021 and references therein). Because samples of the upper mantle, abyssal peridotites, are scarce, the composition of the sub-ridge mantle has primarily been examined by analyzing MORB. On a local scale, the geochemistry of MORB is determined by the inherent heterogeneity of the sub-ridge mantle and the local melting conditions, i.e., the average pressure and extent of melting (e.g., Klein and Langmuir, 1987; Sinton and Detrick, 1992; Rubin and Sinton, 2007; Rubin, 2016).

On a regional scale, MORB composition is influenced by spreading rate (e.g., Allègre and Rousseau, 1984; Batiza, 1984; Langmuir et al.,1992), nearby hot spots (e.g., Schilling, 1991), or large-scale differences in mantle composition (e.g., Dupré and Allègre, 1980; Hamelin and Allègre, 1985; Mahoney et al., 1989; Stracke et al., 2022). Hence, MORB heterogeneity results from a complex interplay of intrinsic factors, including temperature (which controls the depth and extent of melting) and the nature and origin of heterogeneous mantle components on different scales. Superimposed parameters, such as spreading rate, determine the mantle upwelling rate, and thus the rate of melt production which, in turn, influences how melts from heterogeneous mantle components migrate, and mix before eruption on the ocean floor. Hence, spreading rate governs the style of melt accretion and the corresponding lithological and compositional structure of the oceanic crust. The

---

variability of major and trace element concentrations, and isotope ratios of MORB, for example, decrease within individual ridge segments as spreading rate increases (e.g., Allègre and Rousseau, 1984; Stracke et al., 2003; Rubin and Sinton, 2007), showing that compositional homogenization is more efficient at intermediate to fast spreading ridges, where magma supply is abundant.

In contrast, in regions with lower melt production, i.e., at slow spreading rates and/or where the mantle is cold, low magma supply limits melt mixing. Under such conditions, melts from individual mantle components are less likely to be overprinted by mixing with melts from other components. Moreover, preferential melting of mantle lithologies with low solidus temperature dominates the incompatible element budget of the erupted basalts in magma-poor ridge sections (Morgan & Morgan, 1999; Ito and Mahoney, 2005; Stracke, 2008, 2012; Stracke and Bourdon, 2009; Lambart et al., 2019). Magma production may not only vary on a global, but also on a regional or local scale due to differences in mantle temperature and/or spreading rate (e.g., Klein et al., 1991; Graham, 2002; Niu and Batiza, 1994; Niu and Hékinian, 1997; Niu and O'Hara, 2008; Mallick et al., 2019).

At ridge-transform intersections (RTIs), for example, the leading edge of a ridge segment cools as it approaches the lithosphere of the older, colder, opposing plate, resulting in mantle cooling and reduced melt production (e.g., Schilling et al., 1983; Bonatti et al., 1993, 2001; Ligi et al., 2002, 2005; Pickle et al., 2009, Luo et al., 2021). This effect is especially pronounced at RTIs of long-offset, slow-slip transform faults (e.g., Bonatti et al., 1993; Ligi et al., 2005). Here, magmatism is reduced, and basalts become more incompatible element enriched near the transform fault (Ligi et al., 2005). Locally, large-offset multi-fault transform systems are divided in short ridge segments, also called intra-transform ridges (ITRs). Well-studied ITRs are those of the St. Paul (Mid Atlantic Ridge, MAR) and Garret Fracture Zone (East Pacific Rise, EPR), both characterized by three volcanic ITRs that are between 5 and 30 km long and separated by four active transform faults (Niu and Hékinian, 1997; Wendt et al., 1999; Grevemeyer et al., 2002; Hekinian, 2014; Maia et al., 2016; Vincent et al., 2023; Graham and Michael, 2021). Another example is the Quebrada/Discovery/GoFar (QDG) transform system along the EPR that includes eight 5–70 km long ITRs (Pickle et al., 2009). Basalts found at the QDG are variably incompatible element enriched, in contrast to the relatively homogeneous, i.e., well-mixed, basalts from the adjacent ridges (Pickle et al., 2009). Distinguishing mantle source heterogeneity from process-related variations of erupted basalt compositions, which are caused by variable partial melting, melt migration, melt-rock interactions, melt mixing, and magma differentiation, remains a challenge (Rubin et al., 2009, Stracke, 2012, 2021). Intra-transform spreading centers are unique settings where comparatively low melt production may limit melt mixing and thus reduce homogenization of the melts prior to eruption, which therefore may be more heterogeneous than MORB along the major ridge axis.

In this study we present new geochemical and Sr-Nd-Pb-Hf isotopic data of basalts and basaltic glasses from the Doldrums Fracture Zone in the equatorial Atlantic at 7–8°N. The Doldrums transform system is a 110 km-wide multi-fault shear zone, with five active transform faults separated by four short ITRs (Skolotnev et al., 2020; Sani et al., 2023). We present thermal models of the sub-ridge mantle, which suggest a sharp decrease in mantle temperature in the central portion of the Doldrums transform system, causing small degrees of melting beneath the mantle under the central ITRs. Consistent with the thermal models, the basalts from the central ITRs are selectively enriched in incompatible elements. But their low Sr and Pb isotope ratios indicate a lack of incompatible element enriched components in the rising mantle beneath these spreading segments, suggesting prior depletion of such components during melting under the Mid Atlantic Ridge before migrating into the transform domain. The basalts from the ITRs are therefore low degree melts from cold, and mostly peridotitic mantle, with limited overprinting by melts from incompatible element enriched, recycled crust. The example of basalts from the Doldrums Fracture Zone and the

adjacent Mid Atlantic Ridge shows that on-axis MORB generally convey a limited range of the heterogeneity of the sub-ridge mantle. Hence capturing the full extent of mantle heterogeneity requires sampling and analyzing basalts produced under different conditions and in different tectonic settings along Earth's Mid-Ocean Ridge system.

2. Materials and methods

2.1. Geological setting and sample selection

In the equatorial sector of the Atlantic, several long-offset transforms displace the MAR up to 2000 km eastwards. Some of them do not follow a single strike-slip fault along a small circle path relative to the Euler pole of the involved plates (Wilson, 1965; Fox & Gallo, 1984; Carbotte et al., 2016; Karson, 2020). Instead, they are characterized by broad (>100 km), complex multi-fault shear systems, which are up to ~900 km long (e.g., Ligi et al., 2002; Maia et al., 2016; Skolotnev et al., 2020), and often referred to as "mega-transforms" (after Ligi et al., 2002).

In this study, we investigate basalts from the Doldrums transform system, located at 7–8° N. During the 2019 expedition (S45) of the *R/V A.N. Strakhov*, high-resolution multibeam bathymetry was acquired, and rock samples were collected to augment samples from earlier expeditions (*R/V A.N. Strakhov* S06 and S09). Expedition S45 surveyed the entire transform domain, showing a very complex, ~100 km wide deformation zone, considerably deeper than the adjacent MAR segments to the east and west of the transform zone (Skolotnev et al., 2020). This transform system offsets the MAR by 590 km corresponding to a total age difference of ~40 Ma (Fig. 1), featuring five transform faults connected by four 16 to 40 km long spreading centers (Skolotnev et al., 2020).

The new multi-beam data and rock samples, which range from peridotite to gabbro and basalt, have revealed a complex tectonic evolution of the four intra-transform spreading centers, hereafter referred to as ITR-1, ITR-2, ITR-3, ITR-4, from west to east (Fig. 1). The peripheral intra-transform ridge segments, namely ITR-1 and ITR-4, are shallower (~ 4100 m) than those located in the central part (ITR-2 and ITR-3). The latter, ITR-2 and ITR-3, have some of the deepest ridge axes in the equatorial MAR, reaching ~ 4600 m below sea-level (Skolotnev et al., 2020, 2022), and are only 16 and 27 km long. ITR-3 is the shortest and deepest ridge segment of the region. Based on its morphological characteristics, the formation of ITR-3 appears to be associated with the development of an intra-oceanic pull-apart basin within a *transtensional* tectonic regime (Skolotnev et al., 2020). On the other hand, ITR-1 and ITR-4, with lengths of 55 km and 35 km, have broad rift valleys, narrow neo-volcanic axial zones and the lower crust and upper mantle are exposed at their inside corner highs (Skolotnev et al., 2020).

In addition to basalts from expedition S45, samples dredged during expeditions S06 and S09, which extend from the western segment of the MAR (8–9° N) to the southernmost part of ITR-1, are investigated in this study. This sample set covers the entire transform domain, and the neighboring western and eastern MAR segments. The samples from the eastern MAR segment were recovered during expedition S22 with the *R/V A.N. Strakhov* (Fig. 1). In total, 63 basalts were investigated, extending from 6°N to 9.8°N along the MAR. We report major and trace element compositions for these samples, and Sr, Nd, Hf, and Pb isotope ratios for a subset of 41 samples.

2.2. Analytical techniques

The major element composition of fresh glasses was measured by electronprobe microanalysis (EPMA) with a JEOL JXA 8200 Superprobe at the Department of Earth's Science Ardito Desio of Milano University. The analyses of all elements were performed with an accelerating potential of 15 kV, a beam current of 15nA, and a total 30-second counting time. The trace element composition of the basaltic glasses was determined by laser ablation ICP-MS using a QQQ-ICP-MS Agilent Series
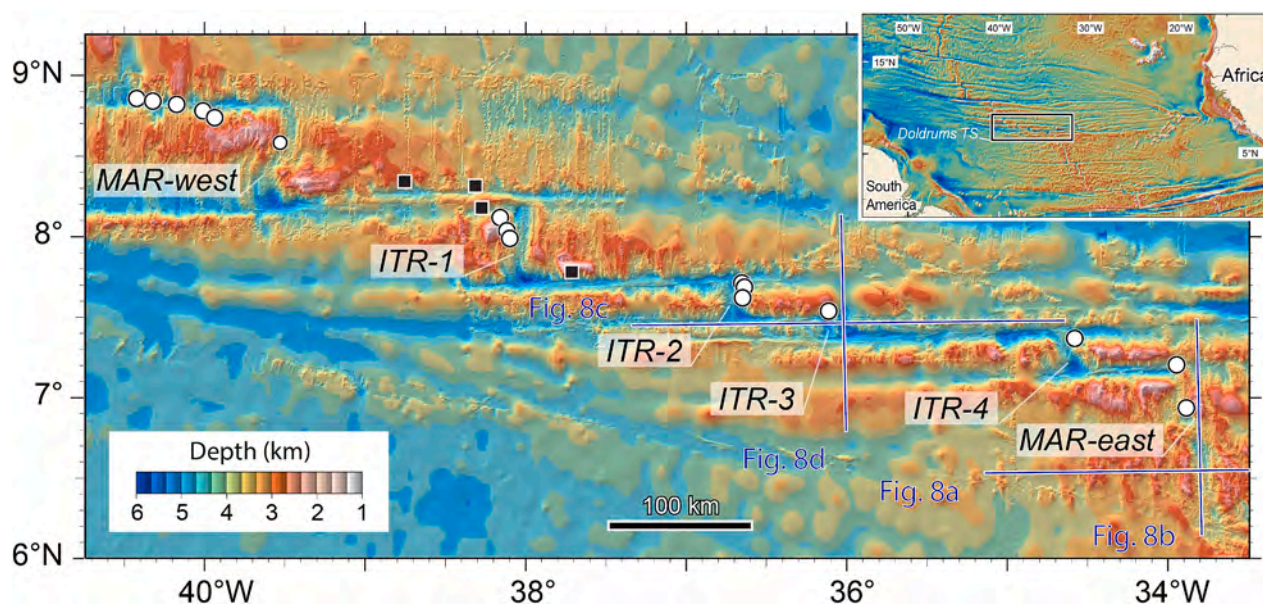
Fig. 1. (a) Bathymetric map of the Doldrums transform system. Shaded relief image based on a compilation of our multibeam data (cruises. S06, S09 and S45) combined with GEBCO 2023 global bathymetric grid. The multibeam data were processed by the Kongsberg Neptune package; spatial analysis and mapping were performed using the PLOTMAP package (Ligi and Bortoluzzi, 1989). Stretching from north to south, the Doldrums Transform System encompasses four intra-transform spreading segments (referred to as ITR-1 to ITR-4) separated by five transform faults (referred to as Doldrums-1 to Doldrums-5) named Doldrums, Vernadsky, two currently unnamed fault segments and Bogdanov (Skolotnev et al., 2020, 2022). The white circles on the image indicate the locations of dredging stations where basalts and basaltic glasses were collected and subsequently analyzed in this study. The black squares are dredging locations where abyssal peridotites were collected and subsequently analyzed in Sani et al. (2023). Blue thick lines mark the locations of cross-sections shown in Fig. 8. Inset, satellite gravity imagery over the central and equatorial Atlantic. Free air gravity data derived from satellite altimetry are from the global grid version 32 (https://topex.ucsd.edu/pub/global_grav_1min/; Sandwell et al., 2014).

8900 interfaced to a GeoLas 193 nm excimer ablation system (Lambda Physik, Germany) at the CNR–IGG S.S. of Pavia. The ablation system was operated at a 10 Hz repetition rate, 50 μm spot size, and a fluence of about 9 J/cm^2. Helium was used as carrier gas and mixed with Ar downstream of the ablation cell. The NIST SRM 610 synthetic glass was used as external standard, with ^{44}Ca as internal standard. Precision and accuracy were assessed by repeated analyses of the BCR-2G reference material and agrees generally better than ±10 % with preferred GeoReM values (Jochum et al., 2005; Table S2). Background and signal were measured for about 60s; signal of standards and unknowns were carefully checked, and the raw data were reduced using the software package GLITTER® using the NIST SRM 610 values of Jochum et al. (2011).

Using the method described in Stoll et al. (2008), 11 basaltic powders were transformed into glass chips and their major element concentrations were determined by EPMA (JEOL 8530F Hyperprobe) at the Institut für Mineralogy of the University of Münster, applying the same measurement conditions as those for glasses measured in Genske et al. (2019). Analyses were carried out with a probe diameter of 10 μm, 5nA current and short counting times of 5 s for peak and 2.5 s for background signal. Prior to quantitative analyses all elements were standardized on matrix matched natural (Mg, Si, Al, Ca, Fe, Mn) and synthetic (Ti, Cr) reference materials. The phi-rho-z correction was applied to all data and relative uncertainties on major element oxides are on the order of 1–2 %. To monitor accuracy and precision over the course of this study microanalytical reference materials were analyzed and the results match published values within error. The same samples were then ablated for trace element analysis with a spot size of 80 μm, using a 193 nm ArF excimer laser (Analyte G2, Photon Machines) at a repetition rate of 10 Hz and an energy of 3–4 J/cm^2, connected to a Thermo Scientific Element 2 ICP-MS and using NIST-610 for calibration. Each analysis is the average of 5–8 individual spots per sample. International glass standards BHVO-2G and BCR-2G were analyzed every 10–12 samples to ensure precision and accuracy (Table S2).

The Sr-Pb-Nd-Hf isotope compositions of basaltic glasses and powders were determined at the Institut für Mineralogie, Universität Münster. The materials (~150 mg, glass chips were hand-picked under a binocular microscope) were leached with H_2O_2 in an ultrasonic bath for about 2 h to remove Mn oxide coatings. Subsequently, all sample material was leached in 6 N HCl for about 2h in an ultrasonic bath, followed by leaching in 6 N HCl for about 2h at 100 °C to minimize the effects of seawater alteration. Basaltic glasses and powders were dissolved in concentrated HF: HNO_3 (4:1) for 3 days at 140 °C. After drying the samples at 120 °C they were re-dissolved in about 5 ml of 6 N HCl together with H_3BO_3 at 120°C for one hour and dried down thereafter.

Strontium, the high field strength element (HFSE) and rare earth element (REE) fractions of the samples were separated on standard cation exchange columns (resin Biorad®AG50W-X8, mesh size 200–400 μm). Strontium was further purified from Rb using 300 μL Eichrom Sr-Spec resin (100–150 μm bead size, Argentino et al., 2021). Hafnium was purified from the HFSE fraction using Eichrom® Ln Spec columns (Münker et al., 2001). Neodymium was further purified from the REE fraction using an Eichrom® Ln Spec resin (mesh size 50–100 μm, Pin and Zalduegui, 1997). Lead was extracted and purified with HBr-HNO$_3$ following the protocol given in Todd et al. (2015) using an AG1-X8 100–200 μm mesh anion exchange resin (Lugmair and Galer, 1992). All samples were processed twice through the columns to improve the separation of Pb from the sample matrix.

The Sr, Nd, Hf and Pb isotope ratios were determined on a Thermo Scientific NEPTUNE *Plus* MC-ICP-MS at the Universität Münster. All Sr cuts were measured in 10 ppb solutions and were bracketed by reference material NBS987. All data were normalized to NBS987 ^{87}Sr/^{86}Sr = 0.710248 (Weis et al., 2006). The USGS rock standards BHVO-2 and BCR-2 gave ^{87}Sr/^{86}Sr = 0.703495 ± 15 (2 S.E.) and ^{87}Sr/^{86}Sr = 0.705020 ± 6 (2 S.E.). The JNdi-1 (20 ppb) Nd bracketing standard was determined at ^{143}Nd/^{144}Nd = 0.512067 ± 11 (2SD, n = 7), and all data are normalized to JNdi-1 ^{143}Nd/^{144}Nd = 0.512115 (Tanaka et al., 2000). The USGS rock standards BHVO-2 and BCR-2 were also measured for

^{143}Nd/^{144}Nd and were determined for BHVO-2 at ^{143}Nd/^{144}Nd = 0.512981 ± 18 (2 S.D., n = 8) and for BCR-2 at ^{143}Nd/^{144}Nd = 0.512641 ± 12 (2 S.D., n = 5). Repeated measurements of the JMC-475 Hf bracketing standard gave an average ^{176}Hf/^{177}Hf = 0.282160 ± 13 (2 S. D., n = 8, 10–30 ppb solutions). All sample data are normalized and reported relative to ^{176}Hf/^{177}Hf = 0.282160 (Blichert-Toft and Albarède, 1997). To verify the accuracy throughout the chromatographic column separation procedure during this study, USGS rock reference materials BHVO-2 and BCR-2 were processed as unknowns and gave ^{176}Hf/^{177}Hf = 0.283096 ± 25 (2 S.D., n = 12) for BHVO-2 and ^{176}Hf/^{177}Hf = 0.282867 ± 20 (2 S.D., n = 10) for BCR-2. For the Tl-doped Pb isotope analyses via MC-ICP-MS accuracy and precision was verified by analyses of BCR-2 and BHVO-2. Lead isotope ratios of BCR-2 gave ^{206}Pb/^{204}Pb = 18.7718 ± 22 (2 S.E.), ^{207}Pb/^{204}Pb = 15.6374 ± 18 (2 S.E.), and ^{208}Pb/^{204}Pb = 38.7824 ± 47 (2 S.E.). Lead isotope measurements of BHVO-2 gave ^{206}Pb/^{204}Pb = 18.6730 ± 17 (2 S.E.), ^{207}Pb/^{204}Pb = 15.5668 ± 16 (2 S.E.), and ^{208}Pb/^{204}Pb = 38.3185 ± 42 (2 S.E.). All sample data are given in Table S3.

2.3. 3D Mantle thermal model

The generation of new oceanic crust along mid-ocean ridges involves a series of interconnected processes, including mantle flow, partial melting, melt segregation, crust formation, and cooling. The dynamics of these phenomena are influenced by the thermal structure beneath mid-ocean ridges, which are primarily controlled by plate movement and ridge-axis discontinuities, such as transform faults. In our study, we employed the numerical model developed by Ligi et al., 2005 to reproduce the 3D mantle thermal model of the Doldrums region and to predict relationships between mantle temperature, melting processes, crustal thickness, and the geochemistry of the oceanic crust within the Doldrums transform system. The details of the methodology can be found in Ligi et al. (2005, 2008). In order to minimize side-edge effects within the study area, we expanded the domain of the numerical experiment to cover a sector of the equatorial Atlantic, ranging from 5.5°N to 14.5°N in latitude and from 56.6°W to 19.8°W in longitude. For accurate delineation of plate boundaries, a combination of global free air anomaly data and bathymetry data was employed, incorporating our own multibeam data and the GEBCO 2023 global grid dataset (Fig. 1). The temperature field before the onset of melting was determined by solving the steady-state advection–diffusion equation, as outlined below.

Mantle flow velocities were estimated assuming steady-state plate thickening passive flow adopting the model of Ligi et al. (2008). The corner flow induced by seafloor spreading was predicted in a computational frame 2048 × 1024 km in width and 150 km in depth, with grid points spaced 1 × 1 × 1 km apart, assuming an incompressible, homogeneous, isoviscous mantle beneath the present plate boundary geometry of the equatorial MAR. The model incorporated variable plate velocities at the base of the rigid plates, deviating slightly from the assumption of rigid plates. This adjustment was made to consider plate velocity variations associated with the distance from the Euler pole, all while applying the flat Earth approximation. Plate velocities were computed on a point-to-point basis using the Euler vector for the South American and Nubian plates, as derived from the MORVEL global plate motions model (DeMets et al., 2010). Along the MAR axis, Nubian plate velocities relative to South America varied from 27.5 mm/yr with an azimuth of 86.4°N to 23.9 mm/yr with an azimuth of 94°N, spanning from the southern- to northernmost edges of the model box. We solved for the steady-state three-dimensional passive mantle flow via a Fourier pseudo-spectral technique (Ligi et al., 2008). The base of the rigid plates, assumed to correspond to the depth of 750 °C isotherm, was obtained iteratively solving each time the mantle temperature field, starting from a constant-thickness plate-flow model (Fig. S1). Computed flow patterns are illustrated in Fig. S2 by contours of velocity component magnitudes at depths of 14 and 35 km, respectively.

Mantle temperatures constituting the 3D thermal model have been computed through a 3D-domain of mantle flow calculations, by the over-relaxation upwind finite difference method described by Morgan and Forsyth (1988), using a variable grid spacing (2048 × 1024 × 101) with the highest grid resolution (1 km) in the proximity of the plate boundaries. Final temperature solutions were found assuming a constant temperature of 0 °C at the surface and 1380 °C at 150 km depth, the lower boundary of the model. The temperature of 1380°C was determined through an iterative process involving three-dimensional calculations of mantle partial melting. The initial basal temperature was systematically adjusted in 30°C increments, starting from 1330°C. This adjustment continued until we achieved a crustal thickness of 6 km at the central regions of the major segments of the MAR stretch under investigation, assuming that all generated melt was successfully extracted. We predicted melt generation by incorporating the influence of water on the peridotite solidus, using the model developed by Ligi et al. (2005, based on a modified version of the parametrization of Katz et al. (2003). We calculated crustal thickness, mean pressure of melting, mean degree of melting, and mean composition of the aggregate melt at various locations along the axis of the ridge segment by integrating the melt production rate over the cross-sectional area where melting occurs (Ligi et al., 2008). This was done for both dry and wet fractional melting models. Our assumptions included mantle mineral assemblages for garnet, spinel, and plagioclase peridotite as outlined by McKenzie and O'nions (1991), with mineral proportions varying linearly from pure garnet peridotite to pure spinel peridotite between 85 and 60 km depth. For the wet melting model, we assumed a water content of 200 ppm in the upper mantle to simulate the 'wet cold conditions' suggested to underlie the equatorial MAR (Ligi et al., 2005).

3. Results

3.1. Chemical and isotopic compositions

All major element concentrations are reported in Table S1. The basalts are tholeiites, with SiO$_2$ from 46 to 52 wt%, and MgO > 6 wt%, with a maximum of 8.5 wt%, and low alkali contents (K$_2$O + Na$_2$O < 4 wt%), with exception of the subalkaline basalts from ITR-3 which have K$_2$O+Na$_2$O up to 4.3 wt%. Basalts from ITR-4 are among the most evolved compositions, with MgO down to 6 wt% but elevated TiO$_2$ of ~2.1–2.3 wt%, (Fig. 2). Generally, basalts from each of the ITRs, or those from a given ridge area, tend to cluster, but do not follow a common fractional crystallization trend. Variable Al$_2$O$_3$ and (CaO/ Al$_2$O$_3$) at similar MgO levels suggest fractional crystallization at various depths under the different ITRs, possibly involving different parental melts (Fig. 2). Nevertheless, basalts from ITR-2 and some of the MAR-east exhibit a common crystallization trend starting from a common parental melt. Specifically, TiO$_2$, Na$_2$O and CaO/Al$_2$O increase, while Al$_2$O$_3$ decreases with decreasing MgO, consistent with olivine and plagioclase fractionation (Fig. 2). Similarly, basalts from ITR-4 and several from the MAR-east segment show similar trends, but displaced to lower Al$_2$O$_3$ (higher CaO/Al$_2$O$_3$) for a similar range of MgO (Fig. 2).

The trace element compositions (listed in Table S2) and shown in Fig. 3 have typical MORB-like patterns with depletions in the most incompatible elements (Rb, Ba, Th, Nb, and light REE (LREE)) compared to the less incompatible elements (Sm, Eu, Gd, Ti, and heavy REE (HREE)). Most samples have HREE contents ranging from 5 to 10 times the values of the primitive mantle (PM), with minimal middle REE (MREE) to HREE fractionation ((Gd/Yb)$_N$ = 1.09–1.25) and LREE depletions relative to the MREE ((La/Sm)$_N$ = 0.7–1.3). Notably, samples from ITR-3 exhibit nearly flat REE patterns, with PM-normalized LREE/ MREE ratios up to 1 (Fig. 3). Additionally, these samples have higher (Nb/Zr)$_N$ and (Zr/Nd)$_N$ compared to the other investigated basalts. Evolved samples from ITR-4 (MgO ~ 6.0–6.5), and a few samples from ITR-2 are depleted in Sr relative to similarly incompatible elements. Samples from ITR-4 and the eastern MAR segment are depleted in K
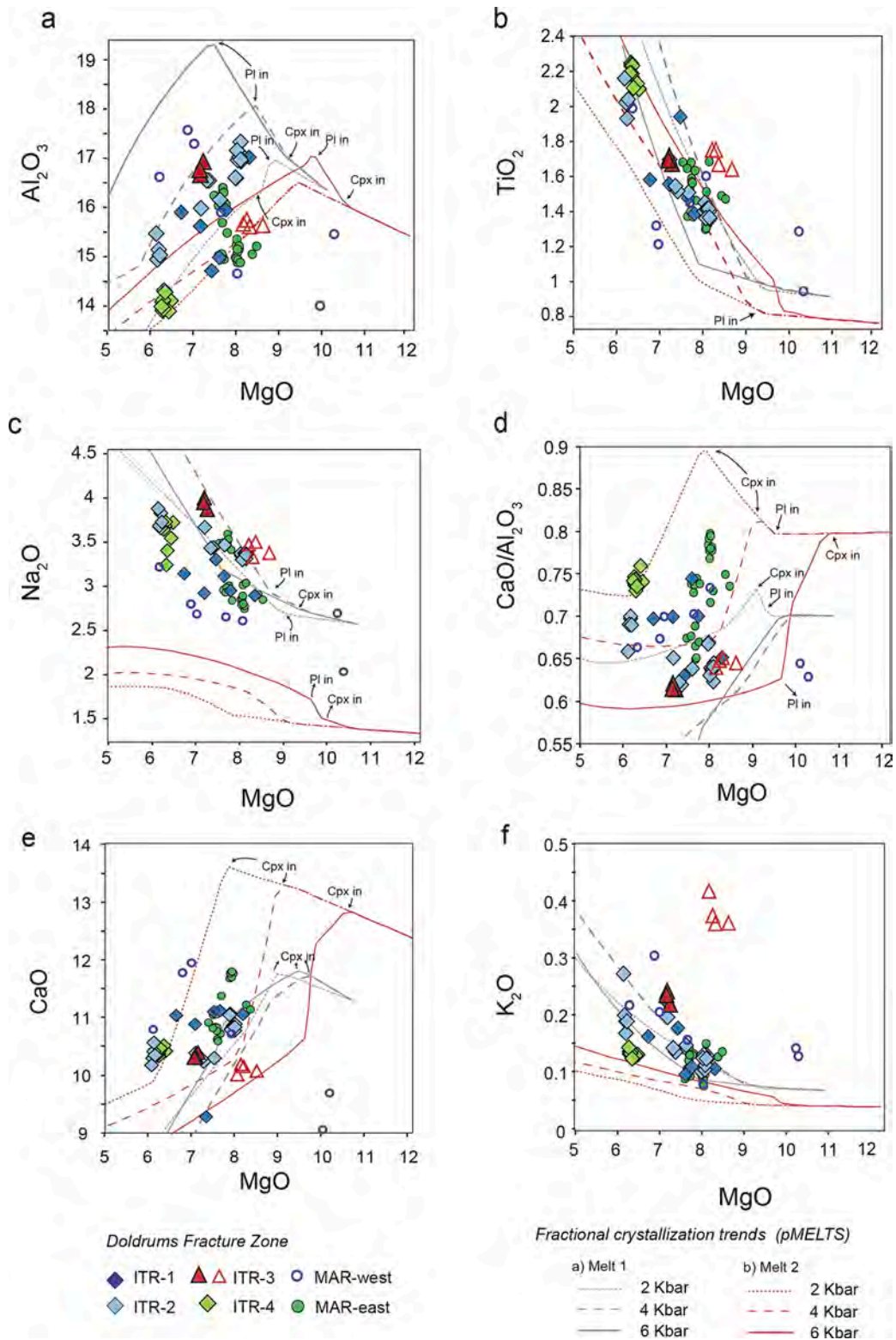
Fig. 2. Variations in MgO wt% versus (a) Al_2O_3 wt%, (b) TiO_2 wt%, (c) Na_2O wt%, (d) CaO/Al_2O_3 wt% ratios, (e) CaO wt% and (f) K_2O wt% of basaltic glasses and whole rock basalts from this study. The latter are represented as empty symbols. In general, whole rock basalts have higher K_2O contents (wt%) compared to the associated basalt glasses, e.g., for samples from the ITR-3. Fractional crystallization trends are shown to evaluate the effect of the different depth of crystallization and the possible parental melt compositions of our samples. Liquid lines of descendent are calculated using the thermodynamic program pMELTS (Ghiorso et al., 2002) through a process of isobaric fractional crystallization starting from a typical mantle potential temperature of ~1325 °C at different pressures (2, 4, 6 Kbar). The compositions used as starting melts are experimental calculations from Kinzler and Groove (1993).
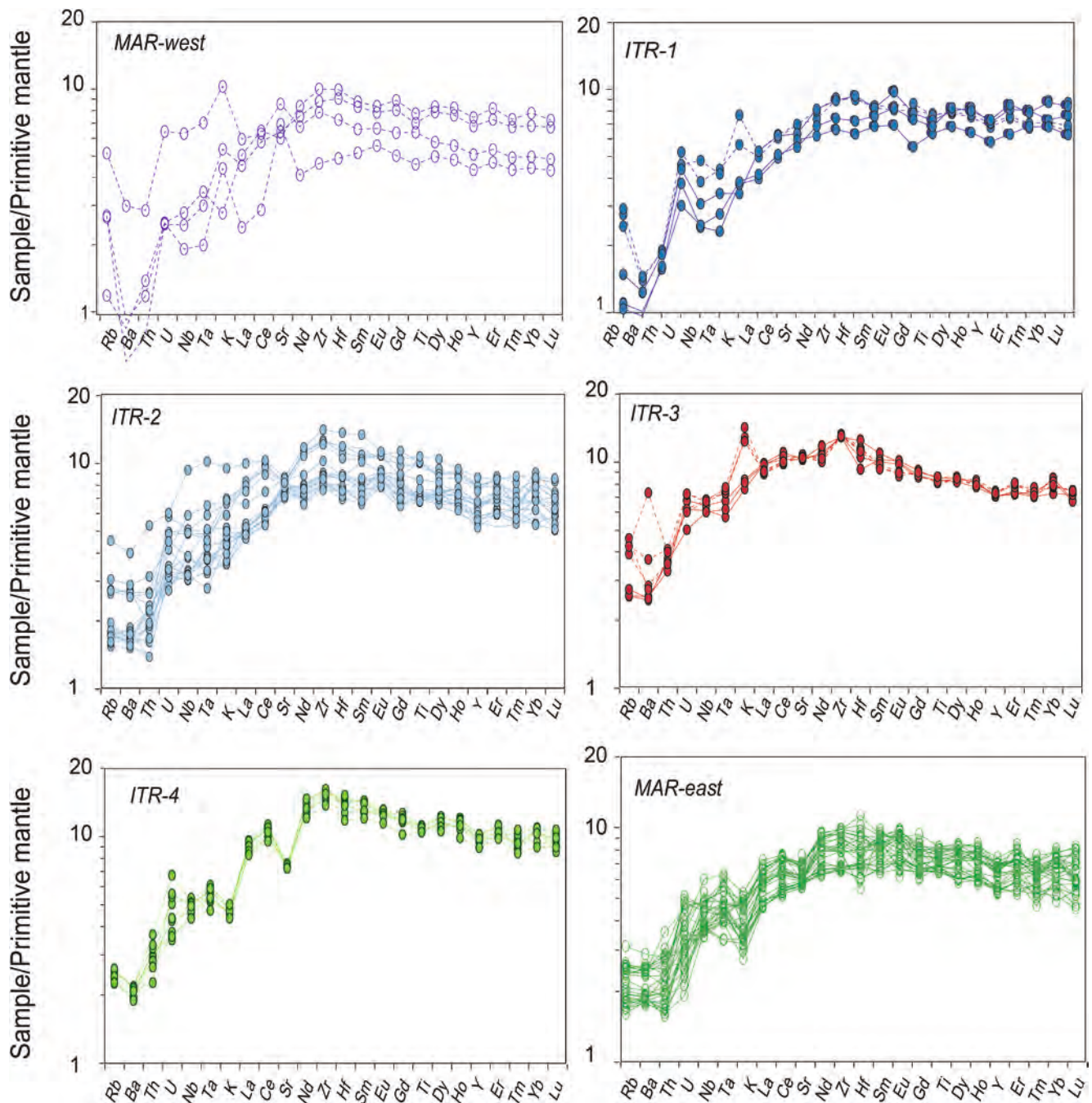
Fig. 3. Primitive mantle-normalized (Sun and McDonough, 1989) diagrams of trace element composition of the studied basalts. Dashed lines refer to basaltic rocks whereas solid lines are basaltic glasses. All trace element abundances depict spoon-shape patterns due to depletion of the most incompatible trace elements (e.g., LILE and LREE) compared to the less incompatible ones (e.g., HREE).

compared to similarly incompatible elements, a feature not observed in the other ITRs and in basalts from the western MAR segment. Also, there is a difference between the glasses and whole rock data from ITR-3; the latter being enriched in Sr, K, Ba, and Rb. This discrepancy may be attributed to the presence of secondary minerals in the whole rock powders, which were avoided during LA-ICPMS analysis of the glasses. During alteration, alkali-rich palagonite is typically the first stable and most common mineral formed, and may explain the alkali enrichment in the crystalline rocks compared to the fresh glasses (Stroncik and Schmincke, 2002). Additionally, the whole rock powders may contain crystalline olivine, in agreement with a higher MgO compared to the basalt glass.

In various combinations of Sr-Nd-Pb-Hf isotope diagrams (Table S3,

Fig. 4), all samples exhibit roughly linear trends between an incompatible element depleted and enriched end-member. Some samples from ITR-2 extend towards higher $^{87}Sr/^{86}Sr$ at nearly constant $^{143}Nd/^{144}Nd$ and $^{176}Hf/^{177}Hf$ ratios. This is a result of seawater alteration, consistent with the presence of abundant palagonite in the glasses at the hand specimen scale.

In Fig. 5, Sr-Nd-Pb isotope ratios are plotted versus $(La/Sm)_N$ and $(Zr/Nd)_N$. Most samples have a similar range of $(La/Sm)_N$ and $(Zr/Nd)_N$ values, but do not correlate with the isotope ratios. Notably, samples from ITR-3 with the lowest $^{206}Pb/^{204}Pb$ and $^{87}Sr/^{86}Sr$ have the highest $(La/Sm)_N$ and $(Zr/Nd)_N$.

Fig. 6 illustrates the chemical and isotopic variations as a function of longitude within the range of 41°W to 33°W, which corresponds to a
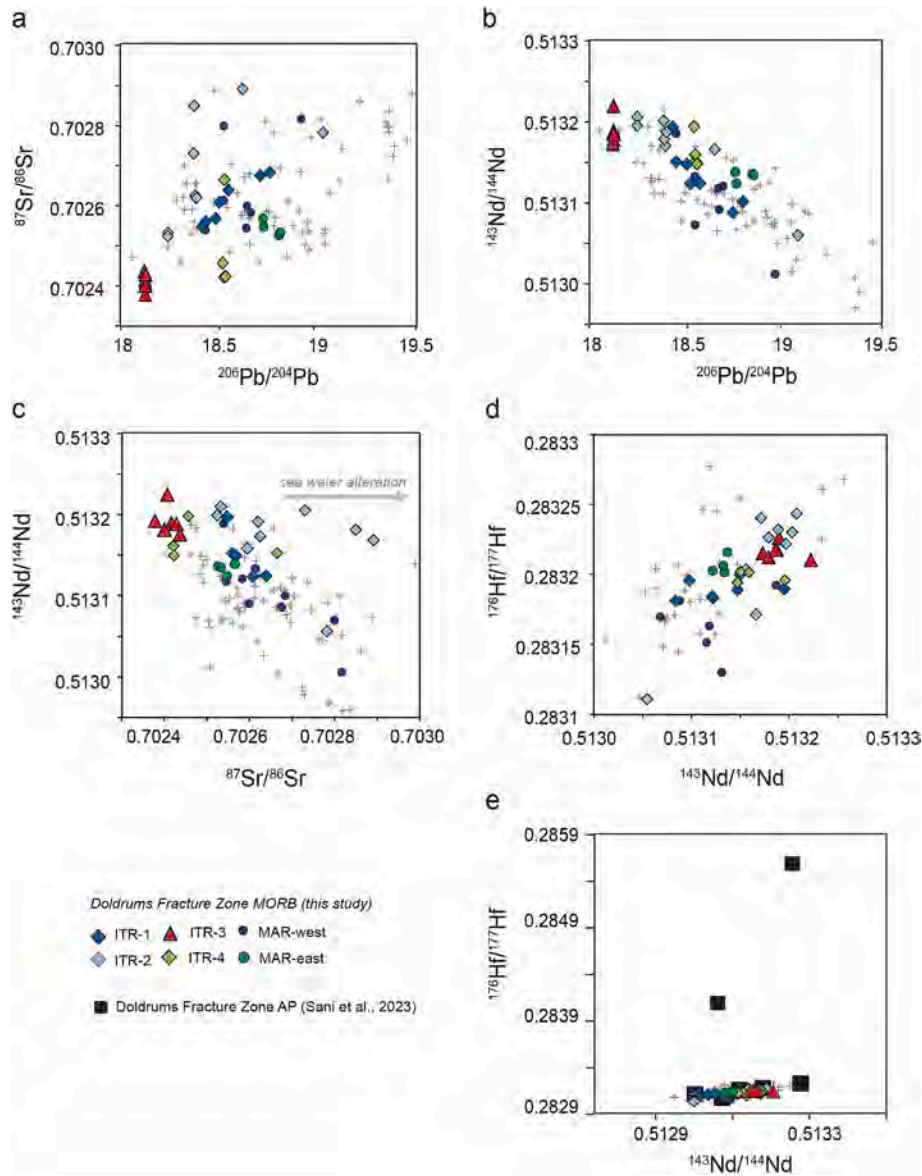
Fig. 4. Sr, Nd, Hf, and Pb isotope ratios of basalts from the studied sector of Mid Atlantic Ridge. Compositions of our samples plot in the field defined by global MORB and range between more isotopically enriched (high Sr-Pb isotopic ratios, low Hf-Nd isotopic ratios) and more depleted compositions (low Sr-Pb isotopic ratios, high Hf-Nd isotopic ratios). Samples from the ITR-3 display the lowest $^{206}Pb/^{204}Pb$ and $^{87}Sr/^{86}Sr$ observed between our samples and in the Equatorial MAR magmatism (panel a, b, c). Samples from the ITR-2 have the highest Nd-Hf isotope ratios and few of them have anomalously high $^{87}Sr/^{86}Sr$ at a constant Pb and Nd isotopic ratios, likely due to seawater alteration. Gray crosses represented MORBs from the Equatorial MAR (−2 to 11°N) (PetDBdataset_PetDB05September2020). In panel e are plotted Hf-Nd isotopic ratios of separated clinopyroxenes from abyssal peridotites collected in the Doldrums transform area (Sani et al., 2023).

latitude between 6.5 °N and 8.9 °N. The Na$_8$ values (Na$_2$O concentrations back-calculated to MgO = 8 wt%, after Klein and Langmuir, 1987) show a slight eastward increase from approximately 2.5 to 3.5, reaching its highest values (3.5–4) at ITR-3. Similarly, the LREE/MREE ratios (i. e., (La/Sm)$_N$) are high in ITR-3 basalts but generally increase from east to west. Despite the local enrichments in LREE and high Na$_8$ values, basalts from ITR-3 have the lowest Sr-Pb isotope ratios observed in the area, but also MORB from the Equatorial Atlantic in general (Fig. 4; e.g. Schilling et al., 1994; Agranier et al., 2005; Kelley et al., 2013; Skolotnev, 2014; Jenner and O'Neill, 2012; Reekie et al., 2019). The Nd and Hf isotopes of ITR-3 basalts, on the other hand, closely resemble those of basalts from the other sectors of the Doldrums transform system, such as those from ITR-2 (Figs. 4 and 6) with values of $^{143}Nd/^{144}Nd$ ratios ranging from 0.5131 to 0.51325 and $^{176}Hf/^{177}Hf$ ratios of 0.28315–0.28325.

3.2. Results from a 3D thermal mantle model

The primary goal of the thermal numerical model was to evaluate the impact of the multi-fault transform system in the Doldrums region on the thermal structure of the underlying mantle. The results of the model are presented in Fig. 7, which displays temperature slices at 20 km, the depth where partial melting typically ends beneath a MAR segment, at 40 km, the mean depth of melting, and at 60 km, the lower boundary of the anhydrous melting region. There is a significant temperature decrease beneath the shorter ITRs segments (ITR-3,4), extending to depths below 60 km. This reduction is primarily attributed to slow mantle upwelling velocities (Figs. S1 and S2) and cold edge effects generated by the long and closely spaced transform faults that bound both ends of these segments. Consequently, these segments exhibit cooler conditions due to conductive cooling, with ITR-3 being the coldest segment. In contrast, the adjacent MAR ridge segments are
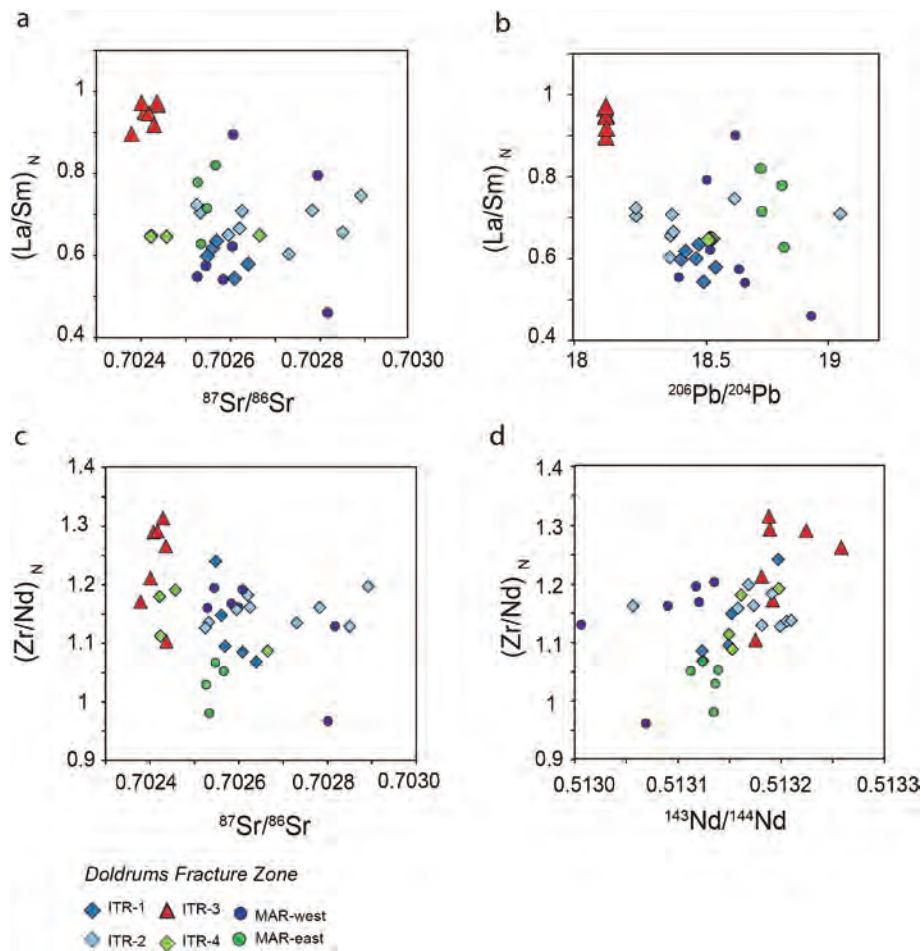
Fig. 5. Trace element compositions versus isotope ratios. The variation of $(La/Sm)_N$ and $(Zr/Nd)_N$ indicates the degree of incompatible element enrichment or depletion. High $(La/Sm)_N$ indicate small degrees of melting (e.g., Stracke and Bourdon, 2009), high $(Zr/Nd)_N$ indicate melting of incompatible element depleted peridotites. Notably, the samples with the highest $(La/Sm)_N$ and $(Zr/Nd)_N$ from the ITR-3 are coupled with the lowest Sr-Pb isotope ratios (a, b, c, d).

longer and not affected by long-offset transform faults, transport mantle material more effectively upwards, and temperature variations are thus dominated by thermal advection.

Fig. 8 includes depth sections illustrating temperature, the melting region, and the degree of melting beneath the MAR segment east of the Doldrums transform system (Fig. 8a, b), as well as beneath the ITR-3 segment (Fig. 8c, d). The across-axis sections cut through the midpoint of the ridge segments (Fig. 8a, c), while the along-axis sections (Fig. 8b, d) follow the ridge axis and intersect the neighboring transform faults. The MAR segment exhibits the expected degree of melting for a slow spreading ridge, with a maximum degree of ~26 % calculated for the central part of the segment and at a depth of ~20 km, a mean degree of melting of ~8–9 % and a crustal thickness of ~6 km. In contrast, the ITR-3 segment reaches a maximum degree of melting of approximately 1–2 % in our model, at a depth of ~50 km, resulting in a crustal thickness of ~1 km.

4. Discussion

4.1. Fractional crystallization

Most of the investigated basalts from within the Doldrums Fracture Zone and the adjacent MAR have MgO between 6 and 8 wt%, indicating small degrees of crystal fractionation. There are several trends of decreasing Al_2O_3 and increasing Na_2O, TiO_2, and K_2O with decreasing MgO, showing that samples from the different localities do not follow a single fractionation path over a similar pressure range, but instead

require that the parental magmas fractionated over different pressure ranges. To test this hypothesis, we used p*MELTS* (Ghiorso and Sack, 1995; Ghiorso et al., 2002) to calculate the liquid lines of descent for two distinct parental magmas at different pressures (Fig. 2). The two parental magmas are primitive melts calculated by Kinzler and Grove (1993) at maximum melting degrees of 10 % (melt 1; MgO = 10.9 wt%) and 20 % (melt 2; MgO = 12.1 wt%) from a depleted mantle source at 15 Kbar. Isobaric fractional crystallization trends at pressures of 2, 4, and 6 kbar, are depicted in Fig. 2. The covariation of Al_2O_3, CaO and CaO/Al_2O_3 with MgO (wt.%) indicates crystal fractionation at variable depths, possibly also involving different parental magmas. The covariation of K_2O, Na_2O and TiO_2 with MgO is also strongly influenced by the parental melt compositions. For both chosen parental magmas, plagioclase fractionation decreases the Al_2O_3 and increases the Na_2O, TiO_2 and K_2O concentrations in the melt during the fractional crystallization process, starting at ~ 9 wt% MgO at 2 Kbar for melt 1, and at 9.7 wt% MgO at 2 and 4 Kbar for melt 2. However, at higher pressure, at 4 and 6 Kbar for melt 1 and at 6 Kbar for melt 2, the major element budget is affected by crystallizing clinopyroxene before plagioclase. In detail, regardless of the initial magma composition, samples from ITR-3, ITR-2 and some from the ITR-1 align along the liquid lines of descent at pressures >2 kbar (Fig. 2a, 2d, and 2e), indicating crystallization depth of more than 6 km. In contrast, some samples from ITR-4 align along liquid lines of descent at pressures of ≤2 kbar (Fig. 2a, 2d, and 2e). In general, the majority of basalts from ITR-1 and from the adjacent MAR segments do not conform to a single fractionation trend (Fig. 2). The parental magmas of the basalts from the Doldrums likely fall between
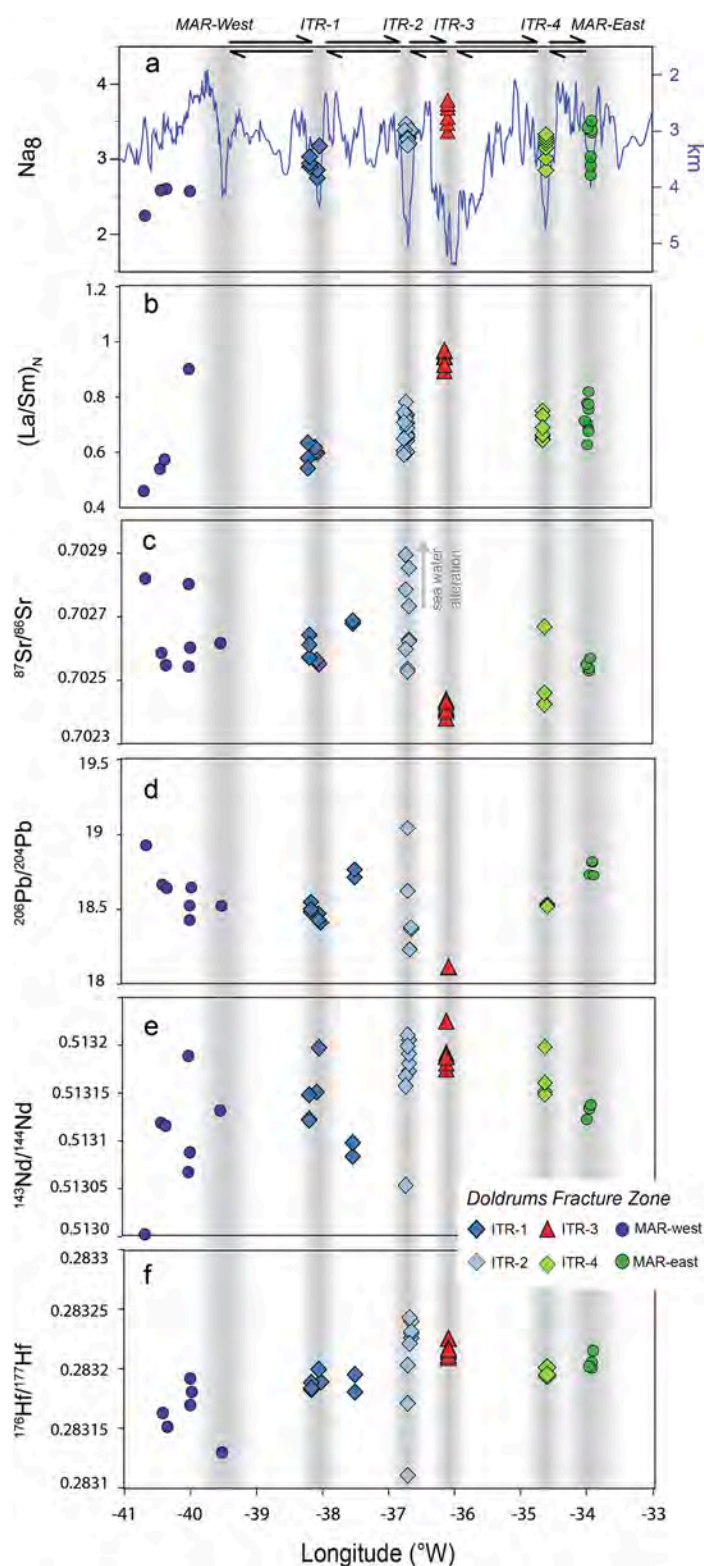
Fig. 6. (a) Na$_8$ values (NaO calculated at 8 wt% MgO, after Klein and Langmuir, 1987) and bathymetric profile reconstructed by blending multiple profiles running parallel to the transform faults that traverse the midpoint of each accretionary segment; (b) (La/Sm)$_N$ ratio; (c) Sr; (d) Nd; (e) Hf and (f) Pb isotope ratios are plotted against longitude for the equatorial MAR between 6°N and 9°N. Different symbols represent individual ridge segments. When moving westward, Na$_8$ values decrease gradually from approximately 3.5 to about 2, while (La/Sm)$_N$ values decrease from 0.7 to 0.5. MORB from ITR-3 have the highest Na$_8$ and (La/Sm)N values, along with the lowest ^{87}Sr/^{86}Sr and ^{206}Pb/^{204}Pb isotope ratios. Meanwhile, ^{143}Nd/^{144}Nd and ^{176}Hf/^{177}Hf show limited variation, indicating minimal compositional changes. Black arrows indicate the active transform faults that separate the ITR segments.

the two chosen starting compositions (i.e., MORB from Kinzler and Grove, 1993).

The basalts from the Doldrums region exhibit varying depths of crystallization depending on their location, suggesting the presence of more than two parental magmas. However, considering that our samples display a limited extent of fractional crystallization (MgO > 6 wt%), crystallization had a limited impact on the trace element compositions and Sr-Nd-Hf-Pb isotope contents of our basalts. Instead, these characteristics are more likely influenced by the style of mantle melting and mantle heterogeneity.

4.2. Melting conditions at intra-transform spreading centers

The great depth of the central ITRs and the development of

detachment faults (Skolotnev et al., 2020; Basch et al., 2022) indicate low/moderate melt supply (Cannat et al., 1996, 2006; Escartín et al., 2008; Smith, 2014) and suggest that magmatism in the central portion of the Doldrums transform system is characterized by limited melt production.

This general view is confirmed by our 3D numerical model which identifies the coldest mantle region under the central Doldrums ITRs (Fig. 7), and the lowest crust production rate at ITR-3 (Fig. 8). However, the passive mantle flow and a homogeneous mantle assumed in the numerical model alone do not explain the long-term persistence of these short intra-transform spreading segments. This is because dynamic mantle flow, driven by buoyancy forces arising from the lower density of residual peridotites (Afonso and Schutt, 2012), and the presence of trapped melt may enhance magma productivity beneath these
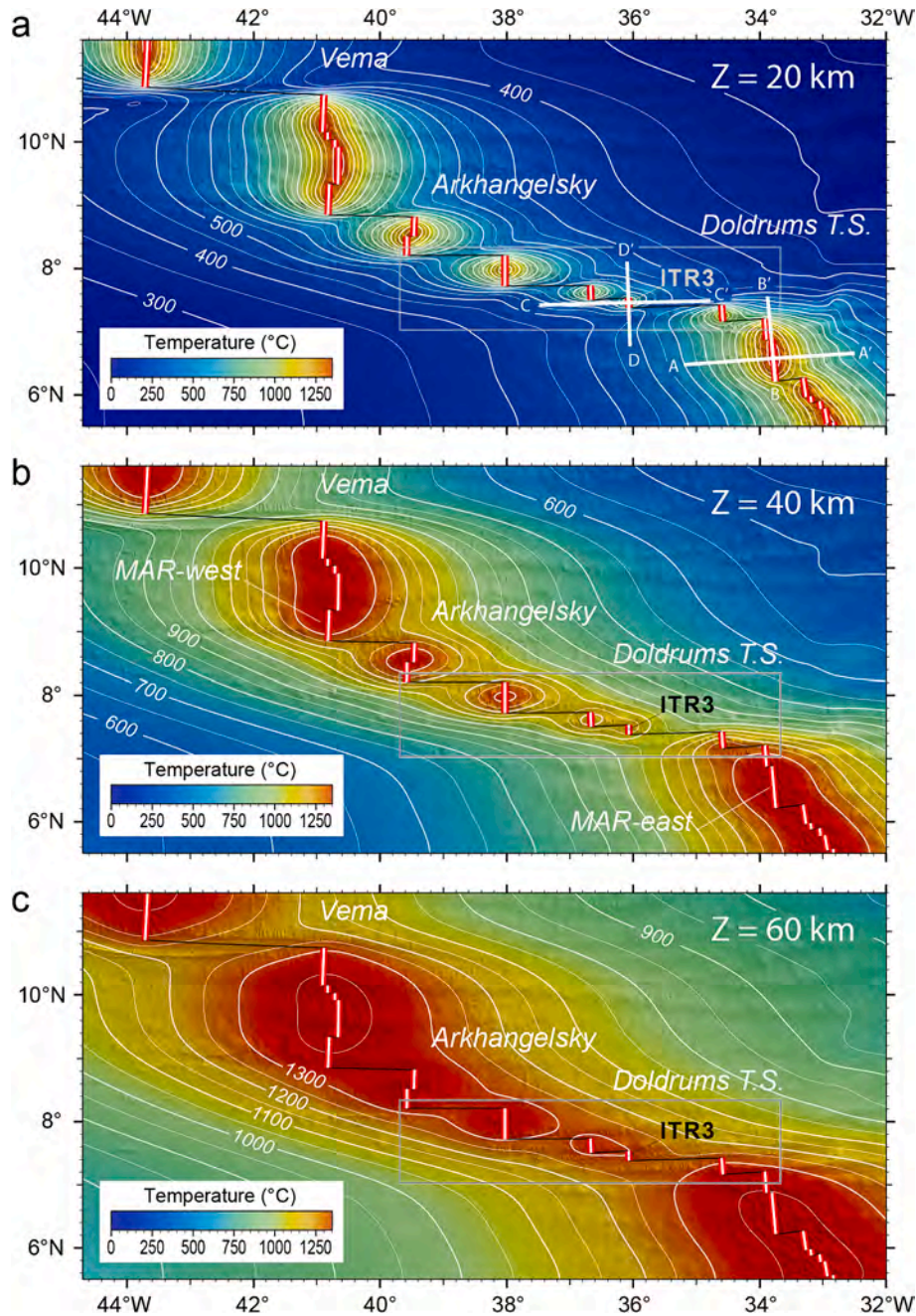
Fig. 7. Predicted mantle thermal structure of the Doldrums region based on 3D modeling results (Ligi et al., 2005, 2008). Temperature distributions at different depths. (a) 20 km, (b) 40 km, and (c) 60 km. Thin white lines represent temperature contours, with increments of 50 °C. White thick lines mark the locations of cross-sections shown in Fig. 8.
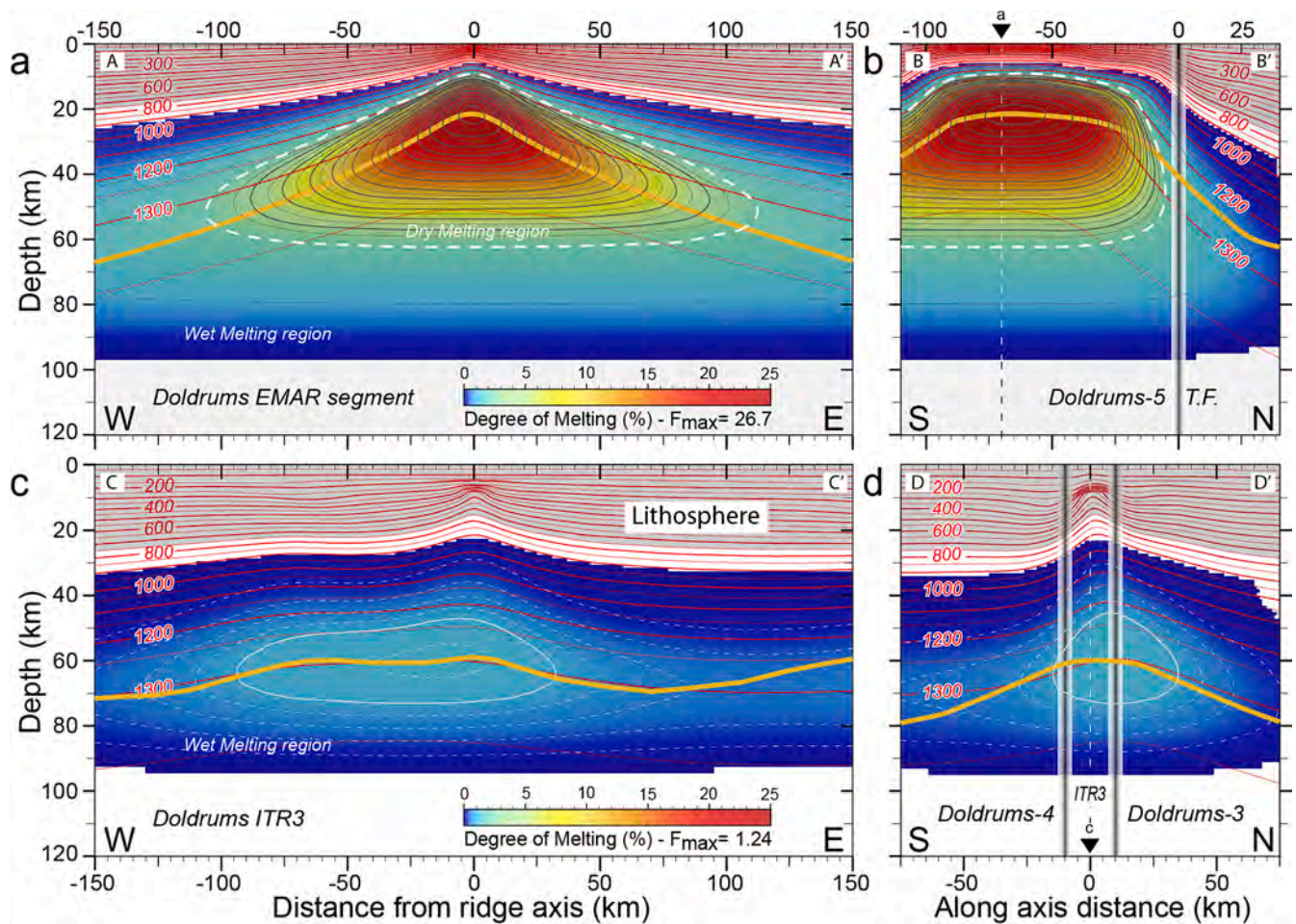
Fig. 8. Melting region and degree of melting inferred for our 3D thermal mantle model (Fig. 7) taking into account the influence of water on the peridotite solidus. Model results are based on the model assumptions, and thus should not be taken to reflect the exact degrees of melting beneath the MAR and ITRs segments in the Doldrums region, but should adequately reflect differences in the average degree of melting under different segments. The fraction of melt generated across (a) and along (b) the axis of the MAR-east ridge segment, and across (c) and along (d) the axis of the intra-transform spreading segment ITR-3. Gray thick lines represent the locations of transform faults bounding the ridge segment, a white dashed line marks the region of dry melting, and a solid thick orange line marks the upper boundary of the region that contributes to melt production. Degree of melting contours, with an increment of 0.5 %, are depicted by black lines. Isotherms are denoted by thin red lines.

exceptionally short ridge segments (Buck & Su, 1989; Scott & Stevenson, 1989; Sotin & Parmentier, 1989). Therefore, our numerical model provides a conservative estimate of the thermal structure beneath the Doldrums transform system. Nevertheless, the major and trace element chemistry of the examined basalts corroborates the scenario predicted by the 3D model, confirming low extents of melting below ITR-3 which produces basalts more enriched in Na_2O, LREE and Zr than the basalts of adjacent MAR segments and nearby ITRs.

The incompatible element enrichment in the ITR-3 basalts, however, is associated with low Sr and Pb isotope ratios, indicating long-term incompatible element depletion of their mantle source (low Rb/Sr and U/Pb). In contrast, MORB samples from other cold environments, specifically at the intersections of long-offset slow-slip transforms with ridge segments, are often incompatible element enriched and have comparatively high Sr and Pb isotope ratios (Bonatti et al., 1993; Schilling et al., 1994; Carbotte et al., 2004; Blichert-Toft et al., 2005). At the Romanche transform fault (0°N along MAR), for instance, basalts from the eastern MAR segment have progressively higher H_2O, Na_8, La/Sm and Gd/Yb approaching the ridge-transform intersection (RTI; Ligi et al., 2005). At the Romanche RTI, melting is confined to the deeper, volatile-rich mantle (Ligi et al., 2005). This deepening of the top of the melting zone is attributed to the "cold-edge effect" that occurs at RTIs, when the warm ridge is juxtaposed to the cold and old lithosphere of the

transform wall. Consequently, the mantle melts deep and to a small extent only, which has the effect that the erupted melts preferentially sample the most incompatible element and H_2O enriched and fusible components of the mantle at the Romanche FZ. This is supported by the high Sr-Pb and low Nd isotope ratios observed of incompatible element enriched MORB from the Romanche FZ (Schilling et al., 1994). Positive, short-scale geochemical and isotopic anomalies are reported from other locations along the MAR, such as at the Chain transform fault (2–3°S along the MAR), where the crustal thickness is lower than the average for slow-spreading ridge. Here, the local high Sr-Pb and low Nd isotope ratios of the basalts also result from preferential melting of small, more fertile heterogeneities than the ambient mantle (e.g. Schilling et al., 1994; Marjanović et al., 2020). Similarly, in the North Atlantic at the Charlie Gibbs FZ (51–53°N along MAR), basalts with high Sr-Pb, and low Nd isotope ratios occur, likely due the preferentially tapping of incompatible element enriched lithologies in the melting process (Blichert-Toft et al., 2005; Skolotnev et al., 2021).

In contrast, basalts from the ITR-3 within the Doldrums transform domain, have low Sr-Pb isotope ratios and moderately high Hf-Nd isotope ratios. Despite the predicted low degrees of melting (Figs. 7 and 8), the mantle component(s) that dominate the incompatible element budget of the ITR-3 melts are therefore not incompatible element enriched as observed at the Romanche, Chain and Charlie Gibbs

FZs, but are rather characterized by lower time-integrated $^{87}Rb/^{86}Sr$ and $^{235,238}U$-$^{232}Th/^{204}Pb$ ratios. The melting characteristics and nature of the mantle source beneath the Doldrums domain, will be investigated further below, using a partial melting and melt mixing model of a heterogenous mantle source.

4.3. Melting a heterogeneous mantle

The upper mantle is a complex amalgamation of various geochemically enriched and depleted components with different isotope ratios, but the exact number and proportion of these components remains unknown. Much of the present-day sub-ridge mantle is incompatible element depleted, as documented by the prevailing incompatible element depletion of its derivative melts, MORB. This incompatible element depletion is acquired during previous melting events. A natural consequence of this prior melting is that the peridotitic mantle is variably incompatible element depleted, because different parts melted to different degrees, as they moved along different paths through the melting region (Langmuir et al., 1992; Stracke et al., 2019; Stracke, 2021). During subsequent residence in the mantle, the most incompatible element depleted peridotites develop high Hf and Nd, but low Sr and Pb isotope ratios that range to values far outside the spectrum covered by MORB (Salters et al., 2011; Stracke et al., 2011, 2019; Byerly and Lassiter, 2014; Willig et al., 2020; Sanfilippo et al., 2019, 2021, 2023; Sani et al., 2023). Peridotites that have melted to a low extent have become only mildly incompatible element depleted, and such peridotites have developed radiogenic isotope ratios similar to MORB, whereas the most incompatible element depleted peridotites have Nd-Hf that are by far higher and Sr-Pb isotope ratios by far lower than any of those observed in MORB (Mallick et al., 2014, 2015, 2019; Willig et al., 2020; Sani et al., 2023). Notably, this intrinsic chemical and isotopic heterogeneity of the peridotitic mantle is an inevitable consequence of prior melting and characteristic of any previously melted, and thus incompatible element depleted peridotitic mantle, i.e., it is an omnipresent feature of the global sub-ridge mantle (Salters et al., 2011; Stracke et al., 2011, 2019, 2021; Willig et al., 2020; Sani et al., 2023).

Locally, abyssal peridotites from the Doldrums region document this expected variable incompatible element depletion and isotopic variability of the sub-ridge mantle (Sani et al., 2023). Some peridotites have clinopyroxenes with extremely high Hf isotope ratios ($^{176}Hf/^{177}Hf$ up to 0.2856), which reflect mantle that has become highly incompatible element depleted by partial melting before ($\gtrsim$1 Ga) recent ridge processing. Other peridotites from the Doldrums region, however, have MORB-like Nd and Hf isotope ratios, showing that the local peridotitic mantle is isotopically highly variable. The Hf-Nd isotopic data of the abyssal peridotites from the Doldrums area are shown in Fig. 4e. For an in-depth discussion of the chemical and isotopic characteristics and evolution of the sub-ridge mantle in the Doldrums region, see Sani et al. (2023).

In addition to its intrinsic chemical and isotopic heterogeneity, the peridotitic mantle also contains interspersed recycled oceanic crust and marine sediments, which are more incompatible element enriched than the peridotitic mantle (Hirschmann and Stolper, 1996; Salters and Dick, 2002; Cipriani et al., 2004; Stracke et al., 2003, 2005;,2012; Chauvel et al., 2008). The main consequence of melting such a lithologically, chemically, and isotopically heterogeneous mantle is that the incompatible element budget of the produced melts (i.e., MORB), and thus also their Sr-Nd-Hf-Pb isotope ratios, are heavily biased toward the composition of the melts from the incompatible element enriched components (e.g., Stracke and Bourdon, 2009; Stracke, 2012, 2021; Brunelli et al., 2018). This also means that melts from the most incompatible element depleted peridotitic portions of the mantle with extreme isotope ratios only have a small influence on the weighted average of the final aggregated melt, i.e., the erupted MORB. Thus, the most extreme isotope ratios of the sub-ridge peridotite are not directly visible in MORB, and MORB do not convey the full diversity of Sr-Nd-Hf-Pb isotope ratios of

the heterogeneous peridotites in the sub-ridge mantle (Salters and Dick, 2002; Stracke and Bourdon, 2009; Stracke, 2012, 2021; Willig et al., 2020).

To account for the compositional and isotopic variability of the peridotitic mantle, we approximate the sub-ridge mantle by three end-members (e.g. Sanfilippo et al., 2019): *1)* ultra-depleted peridotites that are highly incompatible element depleted, *2)* mantle peridotites resembling average depleted mantle (DM) (e.g. Salters and Stracke, 2004), and 3) geochemically and isotopically enriched recycled crust. We calculate the trace element and isotopic compositions of the three end-members and then melt them to different extents, producing three distinct end-member melt compositions.

The trace element and isotopic compositions of the incompatible element enriched recycled crust was calculated by recycling a 2 Ga old oceanic crust plus sediment following the approach described in Stracke et al. (2003). These compositions assume an oceanic crust composed of 50 % gabbro (White et al., 2014), 45 % MORB (Gale et al., 2013), and 5 % altered MORB (Kelley et al., 2003) plus 1 % sediment (GLOSS, Plank and Langmuir, 1998). The melt from the recycled oceanic crust plus sediment, (hereafter referred to as EM-melt) is LREE enriched (La/Sm= 1.83) and has $^{87}Sr/^{86}Sr$ = 0.7032, $^{206}Pb/^{204}Pb$ = 21.1, $^{143}Nd/^{144}Nd$= 0.5129 and $^{176}Hf/^{177}Hf$ = 0.2828. The degree of melting for this pyroxenitic mantle component was calculated based on experiments conducted by Lambart et al. (2009) approximating the degree of melting of the pyroxenite, F_{pyr}, by $F_{pyr} = 0.32 + 4*F_{per}$, with F_{per} being the degree of melting (in %) of DM-like peridotite (Salters and Stracke, 2004) at a mantle potential temperature of 1275°C. We assume F_{per} = 6 % for peridotites, according to the average degree of melting expected in the melting area of Doldrums (calculated by the numerical model shown in Fig. 8) resulting in F_{pyr} ~ 56 % for the pyroxenitic component.

The trace element contents and Sr-Nd-Pb-Hf isotopic compositions of the DM of Salters and Stracke (2004) were used for the moderately depleted peridotitic source component. The resulting melt from this source, hereafter referred to as DM-melt, was generated by melting 6 % (F_{per} = 6 %), consistent with the melting condition of the mantle within Doldrums. The resulting DM-melt has La/Sm = 1.04, which closely matches the average MORB geochemical composition of Gale et al. (2013).

The highly incompatible element depleted mantle component is a residue of partial melting of a DM-like peridotite, generated by extracting 3 % of melt 1 Ga ago, that has developed very high Nd and Hf isotope ratios (Table 1). This ultra-depleted mantle (UDM), despite prior melting, can melt again at typical mantle potential temperatures of ~1325 °C, as demonstrated by previous thermodynamic calculations (Byerly and Lassiter, 2014; Sani et al., 2020), but probably melts to a low extent owing to its depleted nature. We assume, arbitrarily, that the UDM melts to 3 % (Table 1, S4).

4.4. The composition of melts from a heterogeneous mantle

The mixing calculations of the three end-member melts constrain the systematic differences between the different groups of lavas observed in the Doldrums Fracture Zone. A melt mixing grid for mixing melts from UDM, DM and recycled crust (EM-melts) is shown in Fig. 9, further details are given in Table 1 and Table S4.

Generally, basalts from ITR-1, ITR-2, ITR-4 and the majority of the adjacent MAR segments have compositions that cluster along mixing lines between DM and EM-melts (Table 1, and Fig. 9) with EM-melts contributing between <5 % to as much as 20 % (Fig. 9). In contrast, EM-melts contribute <5 % to the ITR-3 basalts with very low Sr and Pb isotope ratios (Fig. 9). The variable deviation from the DM-EM-melt mixing line towards high Hf and Nd isotope ratios in Fig. 9 shows that all samples require small contributions from UDM melts (≲10), with the possible exception of basalts from ITR-3. Given the negligible influence of EM-melts to the ITR-3 basalts, it might be expected that UDM-melts leave a more significant imprint compared to the basalts from the

Table 1

Trace element concentrations and Sr-Nd-Hf-Pb isotope ratios of the mantle end-members and their melts used for the mixing calculations in Fig. 9.

	Enriched mantle source (Stracke et al., 2003)	EM-melt: 56 % F_{Max}	Mantle source-DM mantle (Salters & Stracke, 2004)	DM-melt: 3 % F_{max}	DM-melt: 6 % F_{Max}	Mantle source-UDM mantle (Salters & Stracke, 2004)	UDM-melt: 3 % F_{Max}
Rb	2.73	4.87	0.04	1.40	0.70	0.00000	0.000000
Ba	24.22	43.25	0.57	19.12	9.56	0.00000	0.000000
Th	0.29	0.51	0.01	0.22	0.11	0.00000	0.000000
U	0.09	0.15	0.00	0.08	0.04	0.00000	0.000001
Nb	3.03	5.40	0.10	3.35	1.68	0.00002	0.000732
Ta	0.20	0.35	0.01	0.22	0.11	0.00000	0.000029
La	3.20	5.71	0.23	7.68	3.85	0.00042	0.013894
Ce	9.12	16.28	0.76	23.76	12.67	0.05	1.61
Pb	0.40	0.709	0.02	0.45	0.25	0.002	0.061
Nd	7.56	13.45	0.70	16.88	10.85	0.20	4.89
Sr	123.06	219.74	9.68	257.72	155.12	2.01	53.48
Hf	1.84	3.12	0.20	3.99	2.82	0.09	1.68
Sm	2.50	4.27	0.27	5.12	3.71	0.12	2.32
Gd	3.34	4.84	0.40	5.81	4.58	0.23	3.37
Dy	4.12	4.44	0.53	6.74	5.51	0.34	4.32
Er	2.58	2.002	0.37	3.78	3.24	0.27	2.71
Yb	2.47	1.48	0.40	3.54	3.11	0.30	2.68
Lu	0.37	0.19	0.06	0.51	0.45	0.05	0.40
La/Sm	1.28	1.33	0.84	1.50	1.03	0.00	0.01
^{87}Sr/^{86}Sr	0.7037	0.7037	0.7024	0.7024	0.7024	0.7016	0.7016
^{143}Nd/^{144}Nd	0.5128	0.5128	0.5132	0.5132	0.5132	0.5151	0.5151
^{176}Hf/^{177}Hf	0.2828	0.2828	0.2832	0.2832	0.2832	0.2849	0.2849
^{206}Pb/^{204}Pb	19.91	19.91	18.04	18.04	18.04	14.73	14.73
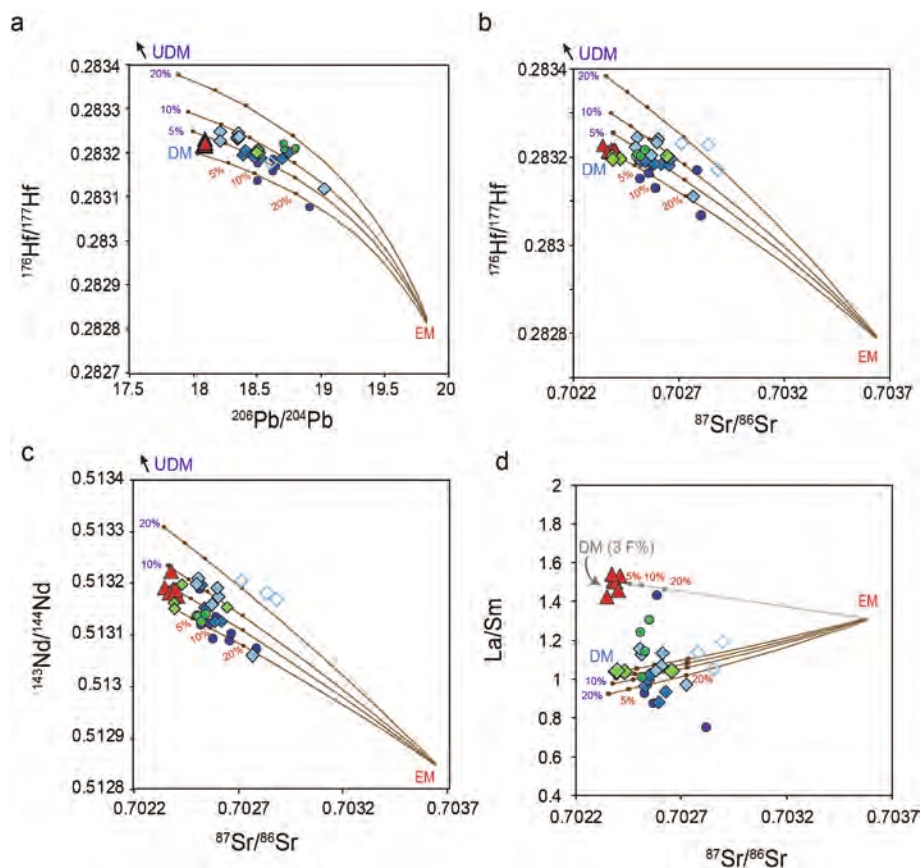
Fig. 9. Presentation of the results of the melt mixing model in Sr-Nd-Pb-Hf isotopic spaces (panels a, b, c) and La/Sm versus ^{87}Sr/^{86}Sr (panel d). Panels a, b, and c show calculated trends of the mixing model with isotope ratios for the three melts labelled (1) DM, (2) UDM and (3) EM. The geochemical and isotopic composition of these melts are reported in Table 1 in the main text. The brown mixing lines represent the mixing between the DM melt and the EM melt. The amount of EM melt participating in the mixing process range here from 5 to 20 % (in red). The blue lines show mixing between DM, EM and UDM melts, with the proportion of the UDM melt from 0 to 20 % (in blue). Panel **d** shows the co-variation of Sr isotope ratios and La/Sm, as indicator of the degree of trace element enrichment. We also show DM-melt produced at low degree of partial melting (~3 %F) mixed with EM melt. Symbols as in Fig. 6. Samples affected by seawater alteration from the ITR-2 are here represented as empty blue-light diamonds.

other ITRs and adjacent ridges (i.e., high Nd and Hf isotope ratios). But the similar values and small variation in Nd-Hf isotope ratios of the ITR-3 basalts compared to those from the other ITRs suggest that UDM-melts seemingly have only a small contribution (Fig. 9). The latter may be a result of the exceptionally cold conditions at ITR-3, which likely prevent melting of the UDM component, such that in absence of significant amounts of EM-melts, the melts generated at ITR-3 are dominated by melts from the DM-like peridotite component (Figs. 8 and 9). The varying contributions of melts from the UDM, DM and EM mantle components to the basalts erupted at the different ITRs in the Doldrums FZ, may therefore reflect the different thermal conditions beneath the different ridge segments (Fig. 7). Based on the mixing model (Fig. 9) and the numerical model of mantle thermal structure (Figs. 7 and 8), it appears that the highly depleted mantle portions with high Hf-Nd isotopes (UDM) are more readily melted in warmer ridge settings, such as those found at the MAR segments, ITR-1, and ITR-4.

The 3D numerical model results (Fig. 8) also suggest that the degree of melting must be significantly lower under ITR-3 compared to both the adjacent MAR segments and the peripheral ITRs (ITR-1, ITR-4), which is in good agreement with the elevated alkali content and high La/Sm observed in ITR-3 basalts. Adopting a lower degree of melting, and therefore higher $(La/Sm)_N$, adequately explains the geochemically enriched but isotopically depleted compositions of the ITR-3 basalts (Fig. 9d, for more detailed information about the underlying calculations see caption of Fig. 9). For simplicity, we present only Sr isotopes versus La/Sm in Fig. 9d and focus solely on mixing between EM-and DM-melts, because in accordance with the cold environment, the melting of highly incompatible element depleted mantle portions (UDM) is suppressed, resulting in a negligible contribution of UDM-melts to the ITR-3 basalts. Although variable contributions of EM-melts to DM-melts could explain the high La/Sm ratios observed in ITR-3 basalts, it would also shift the mixture toward significantly higher Sr (and Pb) isotope ratios. Therefore, in this specific case, the high La/Sm does not reflect the presence of incompatible element enriched mantle heterogeneities. Instead, it suggests low degree melting (~3 %) of a mantle peridotite with DM-like compositions that is almost free of enriched recycled lithologies.

4.5. Mantle re-melting at the intra-transform spreading center

Considering the structural setting of the Doldrums domain and the complex tectonic history that led to the development of the multi-fault transform zone from a single long-offset transform fault (Skolotnev et al., 2020), the apparent lack of melts from recycled crust components (EM-melts) in ITR-3 basalts could be explained if the mantle under ITR-3 was previously drained from such recycled crust components during prior melting under the western MAR axis before moving into the transform domain. The latter is consistent with the westward migration of the MAR inferred from absolute plate motion (Gripp and Gordon, 2002; Doubrouvine et al., 2012; Doglioni et al., 2015; Becker et al., 2015; Wang et al., 2018; Cormier and Sloan,2019; Ligi et al., 2022). A similar scenario has been discussed at the Garret transform (13°30′S, East Pacific Rise, EPR), where basalts from the intra-transform spreading segments have higher Hf and Nd, but lower Sr and Pb isotope ratios than basalts from the adjacent EPR (Wendt et al., 1999; Graham and Michael, 2021). These studies suggested that the mantle within the transform domain had previously undergone melting at the EPR, depleting the most fertile mantle material before remelting within the ITR domain.

4.6. Implications for Mid-Ocean Ridge magmatism

The example of MORB from the Doldrums transform zone shows how the regional and local tectonics along complex transform plate boundaries may control how melts are produced and sample the heterogeneous sub-ridge mantle. The variable pressure and temperature of melt production influence the amount of magma in the sub-ridge mantle, and

thus the style of melt mixing, melt migration, and intrusive versus extrusive magmatism. Within the central Doldrums transform system at ITR-3 cold peridotitic mantle that has previously been deprived in more fusible incompatible element enriched components is melted to small degree leading to limited magma production.

Where the sub-ridge mantle melts to a greater extent, i.e., at the MAR outside the Doldrums transform domain, or along global Mid-Ocean Ridges in general, the generated melts are a complex mix of variable proportions of melts from the local compositionally and lithologically heterogeneous mantle. Along the Juan de Fuca Ridge in the Pacific Ocean, for example, recent on and off-axis volcanism differs in the way they sample local small-scale mantle heterogeneities (Gill et al., 2016). Therefore, it is crucial to explore and study different tectonic settings along Mid-Ocean Ridges to investigate melts formed under different conditions, which reflect a significant part of the compositional heterogeneity of the local mantle, i.e., by sampling off-axis MORB (e.g. Regelous et al., 1999; Cordier et al., 2010; Waters et al., 2011; Gill et al., 2016), adjacent seamounts (e.g., Zindler et al., 1984; Niu and Batiza, 1994; Niu et al., 2002; Brandl et al., 2012), or basalts generated next to or within transform faults (Schilling et al., 1983; Bonatti et al., 1993; Ligi et al., 2002; Pickle et al., 2009).

5. Conclusions

The spatial variation in basalt compositions over a ~300 km section of the Mid Atlantic Ridge at the Doldrums transform domain is attributed to the presence of substantial geochemical and Sr-Nd-Pb-Hf isotopic heterogeneity of the sub-ridge mantle. However, rather than being solely influenced by changes in mantle source composition, the major, trace element, and isotope compositions of basalts within the transform domain vary due to different thermal conditions of the mantle, which, in turn, leads to preferential sampling of specific mantle components. The comparatively low Sr and Pb isotope ratios of the ITR-3 basalts, coupled with enriched LREE and alkalis, are consistent with low degrees of melting of a cold peridotitic mantle source deprived in recycled crustal components. Within the local geodynamic context, the apparent lack of a significant amount of recycled material in the mantle under ITR-3 is likely a result of previous melting under the MAR before laterally moving into the transform domains. Active mantle flow induced by buoyancy forces coupled with the local transtensive tectonics (Skolotnev et al., 2022) may have increased the rate of local mantle upwelling and facilitated renewed partial melting. Due to the cold thermal conditions prevalent in this sector, only the most fertile portions of this sub-ridge mantle, primarily consisting of DM-like peridotites, melted to low degrees ($F_{max} < 6$ %), and prevented re-melting of more refractory peridotitic mantle components (UDM). Hence, basalts generated at ITR-3 mainly reflect melting of a single mantle component, moderately incompatible element depleted, DM-like peridotite (Salters and Stracke, 2004).

On a global scale, however, enriched recycled crustal material and/or ancient, variably refractory peridotites are probably ubiquitous components of the sub-ridge mantle, and may contribute different amounts of melt to the erupted MORB, depending on the local melting conditions of a given ridge segments. The latter are determined mainly by mantle temperature and spreading rate, which together determine the rate of magma production, and thus style of melt aggregation and rate of intrusive versus extrusive magmatism. Sampling a significant extent of the heterogeneity of the sub-ridge mantle therefore requires investigating MORB formed under different conditions, i.e., on and off-axis MORB, local seamounts, or basalts generated next to or within transform faults.

6. Data availability

Data are available through datastore, a service of the University of Münster, at https://doi.org/10.17879/28948482808.

CRediT authorship contribution statement

Camilla Sani: Writing – review & editing, Writing – original draft, Investigation, Formal analysis, Data curation. **Alessio Sanfilippo:** Writing – review & editing, Writing – original draft, Supervision, Methodology, Investigation, Formal analysis, Data curation. **Sergey Skolotnev:** Methodology, Funding acquisition, Data curation. **Marco Ligi:** Writing – review & editing, Writing – original draft, Methodology, Conceptualization. **Felix Genske:** Writing – review & editing, Methodology, Data curation. **Andreas Stracke:** Writing – review & editing, Writing – original draft, Methodology, Data curation.

Declaration of competing interest

The authors declare that they have no known competing financial interests or personal relationships that could have appeared to influence the work reported in this paper.

Acknowledgments

Appendix A. Supplementary material

Fig. S1: Detail of the mantle flow model showing plate boundary geometry and boundary conditions for the Doldrums region. Fig. S2: Mantle flow velocity components for the thickening-plate model at a depth of 40 km.; Table S1: Major element composition of the studied samples; Table S2: Trace element composition of the studied samples and standard measurements and uncertainties. Table S3: Sr-Nd-Pb-Hf isotopic composition of the studied samples. Table S4: Results of the geochemical mixing model. Supplementary material to this article can be found online at https://doi.org/10.1016/j.gca.2024.04.032.

References

Afonso, J.C., Schutt, D.L., 2012. The effects of polybaric partial melting on density and seismic velocities of mantle restites. Lithos 134 (135), 289–303.

Agranier, A., Blichert-Toft, J., Graham, D., Debaille, V., Schiano, P., Albarède, F., 2005. The spectra of isotopic heterogeneities along the mid-Atlantic Ridge. Earth Planet. Sci. Lett. 238 (1–2), 96–109.

Allègre, C.J., Rousseau, D., 1984. The growth of the continent through geological time studied by Nd isotope analysis of shales. Earth Planet. Sci. Lett. 67 (1), 19–34.

Argentino, C., Lugli, F., Cipriani, A., Panieri, G., 2021. Testing miniaturized extraction chromatography protocols for combined $^{87}Sr/^{86}Sr$ and $\delta^{88/86}Sr$ analyses of pore water by MC-ICP-MS. Limnol. Oceanogr. Methods 19 (6), 431–440.

Basch, V., Sanfilippo, A., Skolotnev, S.G., Ferrando, C., Muccini, F., Palmiotto, C., Peyve, A.A., Ermolaev, B.V., Okina, O.I., Ligi, M., 2022. Genesis of oceanic oxide gabbros and gabbronorites during reactive melt migration at transform walls (Doldrums Megatransform System; 7–8°N Mid-Atlantic Ridge). J. Petrol. 63, 1–23.

Batiza, R., 1984. Inverse relationship between Sr isotope diversity and rate of oceanic volcanism has implications for mantle heterogeneity. Nature 309 (5967), 440–441.

Becker, T.W., Schaeffer, A.J., Lebedev, S., Conrad, C.P., 2015. Toward a generalized plate motion reference frame. Geophys. Res. Lett. 42, 3188–3196.

Blichert-Toft, J., et al., 2005. Geochemical segmentation of the Mid-Atlantic ridge north of Iceland and ridge-hot spot interaction in the North Atlantic. Geochem. Geophys. Geosyst. 6 (1), e2023GC010870.

Blichert-Toft, J., Albarède, F., 1997. The Lu-Hf isotope geochemistry of chondrites and the evolution of the mantle-crust system. Earth Planet. Sci. Lett. 148 (1–2), 243–258.

Bonatti, E., Seyler, M., Sushevskaya, N., 1993. A cold suboceanic mantle belt at the Earth's equator. Science 261 (5119), 315–320.

Bonatti, E., Brunelli, D., Fabretti, P., Ligi, M., Portaro, R.A., Seyler, M., 2001. Steady-state creation of crust-free lithosphere at cold spots in mid-ocean ridges. Geology 29 (11), 979–982.

Brandl, P.A., Beier, C., Regelous, M., Abouchami, W., Haase, K.M., Garbe-Schönberg, D., Galer, S.J., 2012. Volcanism on the flanks of the East Pacific Rise: quantitative constraints on mantle heterogeneity and melting processes. Chem. Geol. 298, 41–56.

Brunelli, D., Cipriani, A., Bonatti, E., 2018. Thermal effects of pyroxenites on mantle melting below mid-ocean ridges. Nat. Geosci. 11, 520–525.

Buck, W.R., Su, W., 1989. Focused mantle upwelling below mid-ocean ridges due to feedback between viscosity and melting. Geophys. Res. Lett. 16, 641–644.

Byerly, B.L., Lassiter, J.C., 2014. Isotopically ultradepleted domains in the convecting upper mantle: implications for MORB petrogenesis. Geology 42, 203–206.

Cannat, M., 1996. How thick is the magmatic crust at slow spreading oceanic ridges? J. Geophys. Res. Solid Earth 101 (B2), 2847–2857.

Cannat, M., Sauter, D., Mendel, V., Ruellan, E., Okino, K., Escartin, J., Combier, V., Baala, M., 2006. Modes of seafloor generation at a melt-poor ultraslow-spreading ridge. Geology 34 (7), 605–608.

Carbotte, S.M., Small, C., Donnelly, K.E., 2004. The influence of ridge migration on the magmatic segmentation of mid-ocean ridge. Nature 429, 743–746.

Carbotte, S.M., Smith, D.K., Cannat, M., Klein, E.M., 2016. Tectonic and magmatic segmentation of the Global Ocean Ridge System: a synthesis of observations. Geol. Soc. Lond. Spec. Publ. 420 (1), 249–295.

Chauvel, C., Lewin, E., Carpentier, M., Arndt, N.T., Marini, J.C., 2008. Role of recycled oceanic basalt and sediment in generating the Hf–Nd mantle array. Nat. Geosci. 1 (1), 64–67.

Cipriani, A., Brueckner, H.K., Bonatti, E., Brunelli, D., 2004. Oceanic crust generated by elusive parents: Sr and Nd isotopes in basalt-peridotite pairs from the Mid-Atlantic Ridge. Geology 32, 657–660.

Cordier, C., Benoit, M., Hémond, C., Dyment, J., Le Gall, B., Briais, A., Kitazawa, M., 2010. Time scales of melt extraction revealed by distribution of lava composition across a ridge axis. Geochem. Geophys. Geosyst. 11.

Cormier, M.-H., Sloan, H., 2019. Distinctive seafloor fabric produced near western versus eastern ridge-transform intersections of the northern Mid-Atlantic Ridge: possible influence of ridge migration. Geochem. Geophys. Geosyst. 20, 1734–1755.

DeMets, C., Gordon, R.G., Argus, D.F., 2010. Geologically current plate motions. Geophys. J. Int. 181, 1–80.

Doglioni, C., Carminati, E., Crespi, M., Cuffaro, M., Penati, M., Riguzzi, F., 2015. Tectonically asymmetric Earth: from net rotation to polarized westward drift of the lithosphere. Geosci. Front. 6, 401–418.

Doubrouvine, P.V., Steinberger, B., Trond, T.H., 2012. Absolute plate motions in a reference frame defined by moving hot spots in the Pacific, Atlantic, and Indian oceans. J. Geophys. Res. 117, B09101.

Dupré, B., Allègre, C.J., 1980. Pb–Sr–Nd isotopic correlation and the chemistry of the North Atlantic mantle. Nature 286 (5768), 17–22.

Escartín, J., Smith, D.K., Cann, J., Schouten, H., Langmuir, C.H., Escrig, S., 2008. Central role of detachment faults in accretion of slow-spreading oceanic lithosphere. Nature 455 (7214), 790–794.

Fox, P.J., Gallo, D.G., 1984. A tectonic model for ridge-transform-ridge plate boundaries: implications for the structure of oceanic lithosphere. Tectonophysic 104, 205–242.

Gale, A., Dalton, C.A., Langmuir, C.H., Su, Y., Schilling, J.-G., 2013. The mean composition of ocean ridge basalts. Geochem. Geophys. Geosyst. 14, 489–518.

Genske, F., Stracke, A., Berndt, J., Klemme, S., 2019. Process-related isotope variability in oceanic basalts revealed by high-precision Sr isotope ratios in olivine-hosted melt inclusions. Chem. Geol. 524, 1–10.

Ghiorso, M.S., Sack, R.O., 1995. Chemical mass transfer in magmatic processes IV. A revised and internally consistent thermodynamic model for the interpolation and extrapolation of liquid-solid equilibria in magmatic systems at elevated temperatures and pressures. Contrib. Miner. Petrol. 119, 197–212.

Ghiorso, M.S., Hirschmann, M.M., Reiners, P.W., Kress III, V.C., 2002. The pMELTS: a revision of MELTS for improved calculation of phase relations and major element partitioning related to partial melting of the mantle to 3 GPa. Geochem. Geophys. Geosyst. 3 (5), 1–35.

Gill, J., Michael, P., Woodcock, J., Dreyer, B., Ramos, F., Clague, D., Stakes, D., 2016. Spatial and temporal scale of mantle enrichment at the Endeavour Segment, Juan de Fuca Ridge. J. Petrol. 57 (5), 863–896.

Graham, D.W., 2002. Noble gas isotope geochemistry of mid-ocean ridge and ocean island basalts: characterization of mantle source reservoirs. Rev. Mineral. Geochem. 47 (1), 247–317.

Graham, D.W., Michael, P.J., 2021. Predominantly recycled carbon in Earth's uppermmantle revealed by He-CO_2-Ba systematics in ultradepleted ocean ridge basalts. Earth Planet. Sci. Lett. 554, 116646.

Grevemeyer, I., Schramm, B., Devey, C.W., Wilson, D.S., Jochum, B., Hauschild, J., Weigel, W., 2002. A multibeam-sonar, magnetic and geochemical flowline survey at 14°14'S on the southern East Pacific Rise: insights into the fourth dimension of ridge crest segmentation. Earth Planet. Sci. Lett. 199 (3–4), 359–372.

Gripp, A.E., Gordon, R.G., 2002. Young tracks of hotspots and current plate velocities. Geophys. J. Int. 150, 321–361.

Hamelin, B., Allègre, C.J., 1985. Large-scale regional units in the depleted upper mantle revealed by an isotope study of the South-West Indian Ridge. Nature 315 (6016), 196–199.

Hekinian, R., 2014. Fracture Zones and Transform Faults. Sea Floor Exploration: Scientific Adventures Diving into the Abyss, pp. 255–300.

Hirschmann, M.M., Stolper, E.M., 1996. A possible role for garnet pyroxenite in the origin of the "garnet signature" in MORB. Contrib. Miner. Petrol. 124 (2), 185–208.

Ito, G., Mahoney, J.J., 2005. Flow and melting of a heterogeneous mantle: 1. Method and importance to the geochemistry of ocean island and mid-ocean ridge basalts. Earth Planet. Sci. Lett. 230 (1–2), 29–46.

Jenner, F.E., O'Neill, H.S.C., 2012. Analysis of 60 elements in 616 ocean floor basaltic glasses. Geochem. Geophys. Geosyst. 13, Q02005.

Jochum, K.P., et al., 2005. GeoReM: a new geochemical database for reference materials and isotopic standards. Geostand. Geoanal. Res. 29, 333–338.

Jochum, K.P., Weis, U., Stoll, B., Kuzmin, D., Yang, Q., Raczek, I., Jacob, D.E., Stracke, A., Birbaum, K., Frick, D.A., Günther, D., 2011. Determination of reference values for NIST SRM 610–617 glasses following ISO guidelines. Geostand. Geoanal. Res. 35, 397–429.

Karson, J.A., 2020. Oceanic transform faults. In: Encyclopedia of Geology: Volume 1–6, second edition. Elsevier, pp. 930–946.

Katz, R.F., Spiegelman, M., Langmuir, C.H., 2003. A new parameterization of hydrous mantle melting. Geochem. Geophys. Geosyst. 4 (9), 1073.

Kelley, K.A., Plank, T., Ludden, J., 2003. The composition of altered oceanic crust at ODP sites 801 and 1149. Geochem. Geophys. Geosyst. 4, 8910.

Kelley, K.A., Kingsley, R., Schilling, J.-G., 2013. Composition of plume-influenced mid ocean ridge lavas and glasses from the Mid-Atlantic Ridge, East Pacific Rise, Galápagos Spreading Center, and Gulf of Aden. Geochem. Geophys. Geosyst. 14 (1), 223–242.

Kinzler, R.J., Grove, T.L., 1993. Corrections and further discussion of the primary magmas of mid-ocean ridge basalts, 1 and 2. J. Geophys. Res. Solid Earth 98 (B12), 22339–22347.

Klein, E.M., Langmuir, C.H., 1987. Global correlations of ocean ridge basalt chemistry with axial depth and crustal thickness. J. Geophys. Res. Solid Earth 92, 8089–8115.

Klein, E.M., Langmuir, C.H., Staudigel, H., 1991. Geochemistry of basalts from the Southeast Indian Ridge, 115 E–138 E. J. Geophys. Res. Solid Earth 96 (B2), 2089–2107.

Lambart, S., Laporte, D., Schiano, P., 2009. An experimental study of pyroxenite partial melts at 1 and 1.5 GPa: implications for the major-element composition of Mid-Ocean Ridge Basalts. Earth Planet. Sci. Lett. 288 (1–2), 335–347.

Lambart, S., Koornneef, J.M., Millet, M.A., Davies, G.R., Cook, M., Lissenberg, C.J., 2019. Highly heterogeneous depleted mantle recorded in the lower oceanic crust. Nat. Geosci. 12 (6), 482–486.

Langmuir, C.H., Klein, E.M., Plank, T., 1992. Petrological systematics of mid-ocean ridge basalts: constraints on melt generation beneath ocean ridges. Geophys. Monogr. Ser. 71, 183–280.

Ligi, M., Bortoluzzi, G., 1989. PLOTMAP: Geophysical and Geological Applications of good standard quality cartographic software. Comput. Geosci. 15, 519–585.

Ligi, M., Bonatti, E., Gasperini, L., Poliakov, A.N.B., 2002. Oceanic broad multifault transform plate boundaries. Geology 30, 11–14.

Ligi, M., Bonatti, E., Cipriani, A., Ottolini, L., 2005. Water-rich basalts at mid-ocean-ridge cold spots. Nature 434, 66–69.

Ligi, M., Cuffaro, M., Chierici, F., Calafato, A., 2008. Three-dimensional passive mantle flow beneath mid-ocean ridges: an analytical approach. Geophys. J. Int. 175, 783–805.

Ligi, M., Cuffaro, M., Muccini, F., Bonatti, E., 2022. Generation and evolution of the oceanic lithosphere in the North Atlantic. Riv. Nuovo Cimento 45, 460–533.

Lugmair, G.W., Galer, S.J.G., 1992. Age and isotopic relationships among the angrites Lewis Cliff 86010 and Angra dos Reis. Geochim. Cosmochim. Acta 56 (4), 1673–1694.

Luo, Y., Lin, J., Zhang, F., Wei, M., 2021. Spreading rate dependence of morphological characteristics in global oceanic transform faults. Acta Oceanol. Sin. 40, 39–64.

Mahoney, J.J., Natland, J.H., White, W.M., Poreda, R., Bloomer, S.H., Fisher, R.L., Baxter, A.N., 1989. Isotopic and geochemical provinces of the western Indian Ocean spreading centers. J. Geophys. Res. Solid Earth 94 (B4), 4033–4052.

Maia, M., Sichel, S., Briais, A., Brunelli, D., Ligi, M., Ferreira, N., Campos, T., Mougel, B., Brehme, I., Hémond, C., Motoki, A., Moura, D., Scalabrin, C., Pessanha, I., Alves, E., Ayres, A., Oliveira, P., 2016. Extreme mantle uplift and exhumation along a transpressive transform fault. Nat. Geosci. 9, 619–624.

Mallick, S., Dick, H.J., Sachi-Kocher, A., Salters, V.J., 2014. Isotope and trace element insights into heterogeneity of subridge mantle. Geochem. Geophys. Geosyst. 15, 2438–2453.

Mallick, S., Standish, J.J., Bizimis, M., 2015. Constraints on the mantle mineralogy of an ultra-slow ridge: Hafnium isotopes in abyssal peridotites and basalts from the 9–25 E Southwest Indian Ridge. Earth Planet. Sci. Lett. 410, 42–53.

Mallick, S., Salters, V.J., Langmuir, C.H., 2019. Geochemical variability along the northern East Pacific Rise: coincident source composition and ridge segmentation. Geochem. Geophys. Geosyst. 20 (4), 1889–1911.

Marjanović, M., Singh, S.C., Gregory, E.P.M., Grevemeyer, I., Growe, K., Wang, Z., Vaddineni, V., et al., 2020. Seismic crustal structure and morphotectonic features associated with the Chain Fracture Zone and their role in the evolution of the equatorial Atlantic region. J. Geophys. Res.: Solid Earth 125 (10), e2020JB020275.

McKenzie, D.A.N., O'nions, R.K., 1991. Partial melt distributions from inversion of rare earth element concentrations. J. Petrol. 32 (5), 1021–1091.

Morgan, J.P., Forsyth, D.W., 1988. Three-dimensional flow and temperature perturbations due to a transform offset: effects on oceanic crustal and upper mantle structure. J. Geophys. Res. 93, 2955–2966.

Morgan, J.P., Morgan, W.J., 1999. Two-stage melting and the geochemical evolution of the mantle: a recipe for mantle plum-pudding. Earth Planet. Sci. Lett. 170 (3), 215–239.

Münker, C., Weyer, S., Scherer, E., Mezger, K., 2001. Separation of high field strength elements (Nb, Ta, Zr, Hf): and Lu from rock samples for MC-ICPMS measurements. Geochem. Geophys. Geosyst. 2 (G3).

Niu, Y., Batiza, R., 1994. Magmatic processes at a slow spreading ridge segment: 26 S Mid-Atlantic Ridge. J. Geophys. Res. Solid Earth 99 (B10), 19719–19740.

Niu, Y., Hékinian, R., 1997. Basaltic liquids and harzburgitic residues in the Garrett Transform: a case study at fast-spreading ridges. Earth Planet. Sci. Lett. 146 (1–2), 243–258.

Niu, Y., O'Hara, M.J., 2008. Global correlations of ocean ridge basalt chemistry with axial depth: a new perspective. J. Petrol. 49 (4), 633–664.

Niu, Y., Regelous, M., Wendt, I.J., Batiza, R., O'Hara, M.J., 2002. Geochemistry of near-EPR seamounts: importance of source vs. process and the origin of enriched mantle component. Earth Planet. Sci. Lett. 199 (3–4), 327–345.

Pickle, R.C., Forsyth, D.W., Harmon, N., Nagle, A.N., Saal, A., 2009. Thermo-mechanical control of axial topography of intra-transform spreading centers. Earth Planet. Sci. Lett. 284 (3–4), 343–351.

Pin, C., Zalduegui, J.S., 1997. Sequential separation of light rare-earth elements, thorium and uranium by miniaturized extraction chromatography: application to isotopic analyses of silicate rocks. Analytica Chimica Acta 339 (1–2), 79–89.

Plank, T., Langmuir, C.H., 1998. The chemical composition of subducting sediment and its consequences for the crust and mantle. Chem. Geol. 145 (3–4), 325–394.

Reekie, C.D.J., Jenner, F.E., Smythe, D.J., Hauri, E.H., Bullock, E.S., Williams, H.M., 2019. Sulfide resorption during crustal ascent and degassing of oceanic plateau basalts. Nat. Commun. 10 (1), 82.

Regelous, M., Niu, Y., Wendt, J.I., Batiza, R., Greig, A., Collerson, K.D., 1999. Variations in the geochemistry of magmatism on the East Pacific Rise at 10 30′ N since 800 ka. Earth Planet. Sci. Lett. 168 (1–2), 45–63.

Rubin, K.H., 2016. Mid-ocean ridge magmatism and volcanism. In: Encyclopedia of Marine Geosciences, pp. 1–21.

Rubin, K.H., Sinton, J.M., 2007. Inferences on mid-ocean ridge thermal and magmatic structure from MORB compositions. Earth Planet. Sci. Lett. 260 (1–2), 257–276.

Rubin, K.H., Sinton, J.M., Maclennan, J., Hellebrand, E., 2009. Magmatic filtering of mantle compositions at mid-ocean-ridge volcanoes. Nat. Geosci. 2 (5), 321–328.

Salters, V.J.M., Dick, H.J.B., 2002. Mineralogy of the mid-ocean-ridge basalt source from neodymium isotopic composition of abyssal peridotites. Nature 418, 68–72.

Salters, V.J.M., Stracke, A., 2004. Composition of the depleted mantle. Geochem. Geophys. Geosyst. 5, Q05004.

Salters, V.J.M., Mallick, S., Hart, S.R., Langmuir, C.E., Stracke, A., 2011. Domains of depleted mantle: new evidence from hafnium and neodymium isotopes. Geochem. Geophys. Geosyst. 12, 1–18.

Sandwell, D.T., Muller, R.D., Smith, W.H.F., Garcia, E., Francis, R., 2014. New global marine gravity model from CryoSat-2 and Jason-1 reveals buried tectonic structure. Science 346, 65–67.

Sanfilippo, A., Salters, V.J.M., Tribuzio, R., Zanetti, A., 2019. Role of ancient, ultra-depleted mantle in Mid-Ocean-Ridge magmatism. Earth Planet. Sci. Lett. 511, 89–98.

Sanfilippo, A., Salters, V.J.M., Sokolov, S.Y., Peyve, A.A., Stracke, A., 2021. Ancient refractory asthenosphere revealed by mantle re-melting at the Arctic Mid Atlantic Ridge. Earth Planet. Sci. Lett. 566.

Sanfilippo, A., Liu, C.Z., Salters, V., Mosconi, A., Zanetti, A., Tribuzio, R., 2023. Preserved Nd-Hf-Os isotope variability in replacive channels from the Lanzo ophiolite: traces of incomplete melt aggregation in the shallow mantle. Chem. Geol. 641, 121779.

Sani, C., Sanfilippo, A., Ferrando, C., Peyve, A.A., Skolotonev, S.G., Muccini, F., Zanetti, A., Basch, V., Palmiotto, C., Bonatti, E., Ligi, M., 2020. Ultra-depleted melt refertilization of mantle peridotites in a large intra-transform domain (Doldrums Fracture Zone; 7–8° N, Mid Atlantic Ridge). Lithos 374, 105698.

Sani, C., Sanfilippo, A., Peyve, A.A., Genske, F., Stracke, A., 2023. Earth mantle's isotopic record of progressive chemical depletion. AGU Adv. 4 (2), e2022AV000792.

Schilling, J.G., 1991. Fluxes and excess temperatures of mantle plumes inferred from their interaction with migrating mid-ocean ridges. Nature 352 (6334), 397–403.

Schilling, J.G., Hanan, B.B., McCully, B., Kingsley, R.H., Fontigine, D., 1994. Influence of the Sierra Leone mantle plume on the equatorial Mid-Atlantic Ridge: a Nd-Sr-Pb isotopic study. J. Geophys. Res. Solid Earth 99 (B6), 12005–12028.

Schilling, J.-G., Zajac, M., Evans, R., Johnston, T., White, W., Devine, J.D., Kingsley, R., 1983. Petrologic and geochemical variations along the Mid-Atlantic Ridge from 29°N to 73°N. Am. J. Sci. 283, 510–586.

Scott, D.R., Stevenson, D.J., 1989. A self-consistent model of melting, magma migration and buoyancy-driven circulation beneath mid-ocean ridges. J. Geophys. Res. 94, 2973–2988.

Sinton, J.M., Detrick, R.S., 1992. Mid-ocean ridge magma chambers. J. Geophys. Res. Solid Earth 97 (B1), 197–216.

Skolotnev, S.G., 2014. New isotopic data for Mid-Atlantic Ridge basalts from the Arkhangelsk-Sierra Leone fracture zone (central Atlantic). Doklady Earth Sci. 459 (1), 1429–1435.

Skolotnev, S.G., Sanfilippo, A., Peyve, A.A., Muccini, F., Sokolov, Y.S., Sani, C., Dobroliubova, K.O., Ferrando, C., Chamov, N.P., Palmiotto, C., Pertsev, A.N., Bonatti, E., Cuffaro, M., Gryaznova, A.C., Sholukhov, K.N., Bich, A.S., Ligi, M., 2020. Large-scale structure of the Doldrums multi-fault transform system (7–8°N Equatorial Atlantic): results from the 45th Expedition of the R/V A. N. Strakhov. Ofioliti. 45, 25–41.

Skolotnev, S.G., Dobrolybova, K.O., Peyve, A.A., Sokolov, S.Y., Chamov, N.P., Ligi, M., 2022. Structure of spreading segments of the Mid-Atlantic Ridge between the

Arkhangelsky and Bogdanov Transform Faults, Equatorial Atlantic. Geotectonics 56, 1–20.

Skolotnev, S., Sanfilippo, A., Peyve, A., Nestola, Y., Sokolov, S., Petracchini, L., Dobrolyubova, K., Basch, V., Pertsev, A., Ferrando, C., Ivanenko, A., 2021. Seafloor spreading and tectonics at the Charlie Gibbs Transform System (52–53°N, Mid Atlantic Ridge): preliminary results from R/V AN Strakhov Expedition S50. Ofioliti 46, 83–101.

Smith, D.J., 2014. Clinopyroxene precursors to amphibole sponge in arc crust. Nat. Commun. 5 (1), 4329.

Sotin, C.J., Parmentier, E.M., 1989. Dynamical consequences of compositional and thermal density stratification beneath spreading centers. Geophys. Res. Lett. 16, 835–838.

Stoll, B., Jochum, K.P., Herwig, K., Amini, M., Flanz, M., Kreuzburg, B., Kuzmin, D., Willbold, M., Enzweiler, J., 2008. An automated iridium-strip heater for LA-ICP-MS bulk analysis of geological samples. Geostand. Geoanal. Res. 32 (1), 5–26.

Stracke, A., 2008. Tracking mantle depletion. Nat. Geosci. 1 (4), 215–216.

Stracke, A., 2012. Earth's heterogeneous mantle: A product of convection-driven interaction between crust and mantle. Chem. Geol. 330–331, 274–299.

Stracke, A., 2021. A process-oriented approach to mantle geochemistry. Chem. Geol. 579, 120350.

Stracke, A., Bourdon, B., 2009. The importance of melt extraction for tracing mantle heterogeneity. Geochim. Cosmochim. Acta 73 (1), 218–238.

Stracke, A., Zindler, A., Salters, V.J.M., McKenzie, D., Groenvold, K., 2003. The dynamics of melting beneath Theistareykir, northern Iceland. Geochem. Geophys. Geosyst. 4, 8003.

Stracke, A., Hofmann, A.W., Hart, S.R., 2005. FOZO, HIMU, and the rest of the mantle zoo. Geochem. Geophys. Geosyst. 6 (5), Q05007.

Stracke, A., Snow, J.E., Hellebrand, E., von Der Handt, A., Bourdon, B., Birbaum, K., Günther, D., 2011. Abyssal peridotite Hf isotopes identify extreme mantle depletion. Earth Planet. Sci. Lett. 308 (3–4), 359–368.

Stracke, A., Genske, F., Berndt, J., Koornneef, J.M., 2019. Ubiquitous ultra-depleted domains in Earth's mantle. Nat. Geosci. 12, 851–855.

Stracke, A., Willig, M., Genske, F., Béguelin, P., Todd, E., 2022. Chemical geodynamics insights from a machine learning approach. Geochem. Geophys. Geosyst. 23 (10), e2022GC010606.

Stroncik, N.A., Schmincke, H.U., 2002. Palagonite–a review. Int. J. Earth Sci. 91, 680–697.

Sun, S.S., McDonough, W.F., 1989. Chemical and isotopic systematics of oceanic basalts: implications for mantle composition and processes. Geol. Society, London, Special Publications 42 (1), 313–345.

Tanaka, T., Togashi, S., Kamioka, H., Amakawa, H., Kagami, H., Hamamoto, T., Yuhara, M., Orihashi, Y., Yoneda, S., Shimizu, H., Kunimaru, T., 2000. JNdi-1: a neodymium isotopic reference in consistency with LaJolla neodymium. Chem. Geol. 168 (3–4), 279–281.

Todd, E., Stracke, A., Scherer, E.E., 2015. Effects of simple acid leaching of crushed and powdered geological materials on high-precision Pb isotope analyses. Geochem. Geophys. Geosyst. 16 (7), 2276–2302.

Vincent, C., Maia, M., Briais, A., Brunelli, D., Ligi, M., Sichel, S., 2023. Evolution of a cold intra-transform ridge segment through oceanic core complex splitting and mantle exhumation, St. Paul Transform System, Equatorial Atlantic. Geochem. Geophys. Geosyst. 24 (5).

Wang, S., Yu, H., Zhang, Q., Zhao, Y., 2018. Absolute plate motions relative to deep mantle plumes. Earth Planet. Sci. Lett. 490, 88–99.

Waters, C.L., Sims, K.W., Perfit, M.R., Blichert-Toft, J., Blusztajn, J., 2011. Perspective on the genesis of E-MORB from chemical and isotopic heterogeneity at 9–10 N East Pacific Rise. J. Petrol. 52 (3), 565–602.

Weis, D., et al., 2006. High-precision isotopic characterization of USGS reference materials by TIMS and MC-ICP-MS. Geochem. Geophys. Geosyst. 7 (8).

Wendt, J.I., Regelous, M., Niu, Y., Hékinian, R., Collerson, K.D., 1999. Geochemistry of lavas from the Garrett Transform Fault: insights into mantle heterogeneity beneath the eastern Pacific. Earth Planet. Sci. Lett. 173 (3), 271–284.

White, W.M., Klein, E.M., Holland, H.D., Turekian, K.K., 2014. 4.13-Composition of the oceanic crust. Treatise Geochem. 4, 457–496.

Willig, M., Stracke, A., Beier, C., Salters, V.J., 2020. Constraints on mantle evolution from Ce-Nd-Hf isotope systematics. Geochim. Cosmochim. Acta 272, 36–53.

Wilson, J.T., 1965. A new class of faults and their bearing on continental drift. Nature 207, 343–347.

Zindler, A., Staudigel, H., Batiza, R., 1984. Isotope and trace element geochemistry of young Pacific seamounts: implications for the scale of upper mantle heterogeneity. Earth Planet. Sci. Lett. 70 (2), 175–195.